Borate Polyanions as Cathode Materials for Rechargeable Magnesium-Ion Batteries

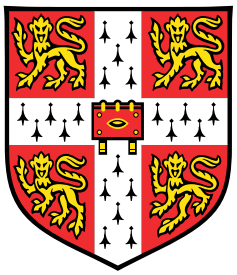

Carson Dermot McLaughlin

Cavendish Laboratory
University of Cambridge

This dissertation is submitted for the degree of
Master of Philosophy

St Edmund's College August 2023

This thesis is dedicated to …

John B. Goodenough, 1922-2023
Airman, Physicist

Declaration

I hereby declare that except where specific reference is made to the work of others, the contents of this dissertation are original and have not been submitted in whole or in part for consideration for any other degree or qualification in this, or any other university. This thesis is the result of my own work and includes nothing which is the outcome of work done in collaboration except where specifically indicated in the text and Acknowledgments. This thesis consists of not more than 15,000 words in length, exclusive of tables, footnotes, bibliography, and appendices.

The views expressed in this thesis are those of the author and do not necessarily reflect the official policy or position of the Air Force, the Department of Defense, or the U.S. Government.

Carson Dermot McLaughlin
August 2023

Acknowledgements

I am grateful for the support and guidance that I have received throughout this journey, without which this MPhil would not have been possible. My sincere thanks go to my supervisor, Professor Siân Dutton, for granting me the opportunity to work in the Quantum Matter group. Her knowledge and insightful questioning provided me with the tools and direction necessary to complete this project. I would like to thank Professor Dame Clare Grey and Dr. Sunita Dey for their scientific guidance. Additionally, I am immensely grateful to Camilla Tacconis, whose hands-on teaching was vital to the project's completion. Finally, I thank Dr. Cheng Liu, who trained me to operate the laboratory equipment used throughout this project.

Abstract

Magnesium-ion batteries are emerging as a promising alternative to lithium-ion batteries due to their superior volumetric capacity, lower cost, and improved safety; however, research is needed to identify an effective cathode and electrolyte. This project investigates the use of borate polyanion systems as intercalation cathodes for next-generation magnesium-ion batteries. Phase-pure $Mg_2Mn(BO_3)_2$ and $Mg_2Ni(BO_3)_2$ samples were prepared using ceramic synthesis and the structure was evaluated using X-ray diffraction (XRD). Suitability for Mg-ion battery usage was evaluated using electrochemical measurements and ex-situ characterization. Lithium iron borate, $LiFeBO_3$, was synthesized and its electrochemical performance was compared to the magnesium-containing orthoborates. When cycled vs. lithium at 55°C, capacities up to 200 $mAhg^{-1}$ were extracted from both magnesium orthoborates on the first charge. Ex-situ scanning electron microscopy-energy dispersive X-ray (SEM-EDX) analysis and synchrotron XRD performed on cells containing $Mg_2Mn(BO_3)_2$ showed no evidence of Mg removal during the first charge. Operando X-ray absorption near edge structure (XANES) spectroscopy on cells containing $Mg_2Mn(BO_3)_2$ also showed no transition metal oxidation during the first cycle. This work demonstrates that despite having high theoretical capacities and proven lithium borate analogs, magnesium orthoborates did not function as magnesium-ion intercalation cathodes under the tested conditions. The capacities achieved by the magnesium orthoborates on first charge exhibited a positive correlation with time spent ball-milling the cathode. Infrared (IR) spectroscopy suggested that the mechanism responsible for the observed capacities could possibly be an amorphous, decomposition product. Further study on the electrochemical properties of borate glasses is necessary to accurately attribute the capacity contributions.

Table of contents

List of figures

List of tables

Nomenclature

Acronyms / Abbreviations

EDX	Energy Dispersive X-ray
IR	Infrared
MPMS	Magnetic Properties Measurement System
SEM	Scanning Electron Microscope
SHE	Standard Hydrogen Electrode
SQUID	Superconducting Quantum Interference Device
XANES	X-ray Absorption Near Edge Structure
XRD	X-ray Diffraction

Chapter 1

Introduction

"If we want to reduce poverty and misery, if we want to give to every deserving individual what is needed for a safe existence of an intelligent being, we want to provide more machinery, more *power. Power* is our mainstay, the primary source of our many-sided energies." - Nikola Tesla

1.1 Research Motivations

The following is a discussion of the motivations for researching new battery technologies. I begin by detailing two case studies which illustrate a problem with the current energy grid. The intermittency of renewable energy sources cannot meet the continuous demand of consumers. Two potential solutions to this problem are: continued reliance on fossil fuels for the majority of energy production or the construction of utility-scale batteries which supply the grid with energy when wind and solar power are unavailable. The United Nations asserts that the second solution is the necessary path to develop as a human civilization [1]. Improved battery technologies will facilitate this energy transition, therefore they must be researched. Additionally, I discuss the growing demand for batteries in electric vehicles and portable electronic devices as motivations for battery research.

In the same way that Immanuel Kant cast aside his preconceived religious notions when formulating deontological ethics in *The Metaphysics of Morals*, I disregard political and social emotions in my discussion in favor of a logic-based approach.

In February 2021, the state of Texas experienced severe winter storms which coated the landscape in ice and delivered temperatures 28°C below average to its 29 million residents [2]. In response to the cold weather, homeowners and businesses throughout the state simultaneously turned up their heating units. This increased energy demand exceeded the available supply, resulting in widespread power outages. In summary, the failure of the

energy grid left 4.5 million people without power, cost the Texas economy an estimated $129 billion, and claimed the lives of 246 human beings [3, 4].

In August 2020, the state of California recorded its hottest temperature since 1913 [5]. To stave off the excessive temperatures, residents turned on their air conditioning units at peak hours. The power companies could not meet this simultaneous demand and were forced to shut off electricity to millions of consumers [6]. This caused uncalculated harm to health, happiness, and economic output. It also interrupted operations in hospitals, nursing homes, and schools. To this day, California leads the United States in power outages because of its insufficient energy generation capabilities [7].

It is apparent from these two examples, and others like them from around the globe, that current energy infrastructure is imperfect. Environmentalists place the blame for these two grid failures on the lack of renewable energy [8]. Many engineers place the blame for these two calamities on an over-reliance on renewable energy [9]. Although seemingly dissonant, these two viewpoints each hold truth, and it is only through careful analysis of both that society can reach a more desirable future.

Environmentalists contend that human greenhouse emissions contribute to climate change and that one consequence of climate change is more extreme weather. This manifests itself as hotter summers, colder winters, and more frequent, powerful storms. They maintain that the frigid cold and searing heat which initiated the crises in Texas and California are examples of the effects of climate change. To mitigate future blackouts, they argue, we should mitigate climate change, and the principle mechanism by which to do that is to transition away from fossil fuels to renewable resources. California governor Gavin Newsom has said, “California is building on our global climate leadership with bold strategies that harness the power of nature to fight climate change and protect our communities and ecosystems” [10]. Similarly, Houston mayor Sylvester Turner has stated, “The storms are coming with greater frequency, greater intensity and costing all of us a lot more. The emphasis is reducing greenhouse gas emissions and creating a more resilient environment” [11]. There is significant scientific research supporting this argument, but any efforts to institute policy change are met with justifiable resistance.

Instead of looking at a nuanced web of cause and effect spun to identify the root of the issue, engineers take a direct approach: the cause of power outages is simply not enough power. Although the heat wave in California and the winter storms in Texas were extreme, they were not unprecedented. It gets hot every summer in California and cold every winter in Texas. The weather has not changed significantly; it can be considered a controlled variable. The thing that has changed is how those two states produce their power. California lawmakers demanded that by 2035, 90% of the state’s energy must come from renewable resources [12].

In 2021, 33.6% of California's power came from renewable resources with solar accounting for over half of that [13]. Similarly, local leaders in Texas have pushed for more renewable energy. Over 20% of power in Texas comes from wind farms [14]. In 2021, Texas led the United States in new renewable energy projects, installing 7352 megawatts of wind and solar energy [15]. The hasty transitions to renewable energy in California and Texas exposed its current limitations.

It is crucial to note that nearly all energy used in households and businesses is produced on demand by power plants. Energy is not stored in reserve, rather it is delivered from the plant to a station, then to consumers. If more energy is demanded, the plants operate at a higher capacity. For this reason, wind and solar power face an inherent obstacle. They cannot be adjusted based on demand; they are controlled by nature. When Californians arrive home at the end of the workday, they turn on their air conditioning, and demand spikes. This coincides with the setting of the sun, thus the loss of solar energy as a source of power. When Texans around the state turned on their heaters, most wind farms were shut down due to the extreme weather. Clearly, an over-reliance on renewable energy sources was a major contributing factor to the catastrophic failures in California and Texas.

If the transition to wind and solar power is to occur, it can only be instituted by two mechanisms: one, supplementation by a network of continual power plants (fossil fuel and nuclear), or two, the storage of wind and solar energy for when the sun does not shine and the wind does not blow, yet the grid still demands power. In the near term, option one will enable the transition, but option two is an inescapable future. The American scientist, businessman, and investor Elon Musk says "It's a definition that if it's not renewable, it's going to run out at some point. And we will have the choice of the collapse of civilization—and into the Dark Ages we go—or we find something renewable" [16]. If one can overlook the bleak, alarmist diction, there is a logical argument at the core of his thought. Regardless of whether human emissions are even affecting the climate, nonrenewable resources will run out, so we need to take the next step as a human civilization. Nuclear energy is a safe, proven option which, like renewables, does not release carbon and, like fossil fuels, can produce energy on demand. Statistically, it has the second lowest death rate per unit of energy production among all sources of energy [17]. Despite this, investment in nuclear energy is bogged down by misinformed fears [18]. Energy storage in flywheels, compressed air, and, most probably, batteries will address seasonal variations and daily load-leveling in renewable energy production. Gas and coal power should be gradually scaled down to allow time for utility-scale battery technology to mature. Batteries will be an effective solution to address the intermittency of renewables. Regardless of the cost or motivations, the transition to

renewable power is a necessary step that can only be enabled by further scientific research into batteries.

Electric vehicles are a second motivation for battery research. The argument that society ought to switch from gasoline automobiles to electric vehicles is supported by two points. One, transportation accounts for 25% of global greenhouse emissions [19]. If society believes it is advantageous to reduce these emissions, then switching to electric cars will achieve this. Two, switching to electric vehicles, along with renewable energy sources, eliminates oil as an instrument of power. The exchange of goods and ideas between countries is indubitably a beneficial endeavor, but when certain states have exclusive control of an essential resource, they can exercise that control to infringe upon the freedom and independence of other reliant states. Since the Second Industrial Revolution, oil has been a foundational element of every large economy. When refined and burned, it transports products and workers by land, sea, and air. It is imbalanced and dangerous for the 13 member states of the Organization of the Petroleum Exporting Countries (OPEC), which hold 82% of the world's oil, to fix the price of a global commodity. In another example, when the European Union (EU) sought to place an embargo on Russian exports as punishment for its 2022-23 war against Ukraine, it could not reach a consensus on oil. This was because eliminating Russian oil would have more adverse effects on the European economy than the intended victim, Russia. It took eleven months for the EU member states to implement a qualified ban on Russian oil, which gave Russia valuable time and money to continue its offensive [20]. Evidently, switching to electric vehicles will both reduce greenhouse gas emissions and increase state autonomy by removing oil as an instrument of power.

This transition to electric vehicles (EVs) can only be implemented by continued research into batteries. Currently, EVs outperform gasoline cars in efficiency and acceleration. On average, EVs convert 77% of the energy in their batteries into usable power at the wheels. Conventional vehicles only convert 12% to 30% of the energy stored in gasoline into power at the wheels [21]. The remainder is primarily lost as heat and sound. Additionally, through a process known as regenerative braking, EVs can improve their efficiency to 90% [22]. This process works by converting the energy lost when slowing down into usable electric energy. When pressing the gas pedal, batteries supply an electric motor with energy to spin the wheels. When braking, this pathway is reversed, so that the spinning of the motor recharges the battery. Electric motors provide EVs with another advantage over conventional gasoline cars: instantaneous torque. The quickest commercially-available gasoline cars go from 0-60 miles per hour in just under 3 seconds. The automobile brand Tesla's quickest EV can do it in under 2 seconds, for a fraction of the cost [23]. This is due to the nature of the motor. When stationary, electric motors produce maximum torque, but as they accelerate a back

electromotive force (emf) inhibits further acceleration. Conversely, the torque delivered by gasoline motors is zero when stationary and increases with increasing speed as the motor burns more fuel. This means EVs are quicker off the starting line, but gasoline cars are faster when measuring top speed.

This difference marks the first of four apparent negative attributes of EVs which could be addressed by better battery technology: speed, range, refuel/recharge time, and lifespan. Firstly, EVs are top-speed-limited to preserve battery life. Secondly, consumers mistrust the range one can travel with a single charge. In 2021, the median range of conventional automobiles on one full tank was 649 kilometers (km) whereas the median range of electric vehicles was only 377 km [24]. EV range can foreseeably attain and surpass gasoline range with improved battery technology. Thirdly, one can refuel a gas car in less than a minute, while it takes hours for EVs to charge fully. Fourthly, EVs have a shorter lifespan compared to most modern gasoline automobiles. Goals set by the United States Advanced Battery Consortium demand a 15-year lifespan and operating temperatures between -30°C and 52°C [25]. This is outside the capability of today's EVs. Evidently, both the invisible hand and an abundance of political and industry leaders are steering transportation to an electric future. The merits of this future include sustainability, efficiency, and acceleration. But, in order to attain and maximize this future, battery research needs to address shortcomings in top speed, range, recharge time, and lifespan.

Battery research is driven not only by emerging markets like grid-scale energy storage and electric vehicles, but also existing markets like portable electronics. Batteries power phones, laptops, hearing aids, and ample other devices which have become essential to everyday life. The global battery market in 2021 was $105.6 billion. It is expected to reach $400 billion by 2030 [26]. This growth will be sustained by continued battery research which improves the abilities of portable electronics.

It is evident that the demand for improved battery technology is present and growing. Before detailing the research on next-generation magnesium-ion batteries which could contribute to the battery industry, it is necessary to explain the fundamentals of battery technology and define relevant terms.

"The pursuit of knowledge is, I think, mainly actuated by love of *power*. And so are all advances in scientific technique." - Bertrand Russell

1.2 Theoretical Background

The following is a discussion of the physical science underlying electric batteries. I detail the earliest known batteries and chronicle how scientists built on the discoveries of the past to arrive at the technology of the present. I describe how the anode, cathode, and electrolyte of a battery commandeer basic chemistry principles to drive electric current through a circuit. Next, I characterize the performance metrics by which batteries are measured and compared. Finally, I communicate the process by which the majority of modern, rechargeable batteries function: intercalation.

In 1936, archaeologists near the ancient city of Ctesiphon, present day Baghdad, unearthed three nested objects: an iron rod inside of a copper cylinder inside of a clay jar. Testing revealed that the jar once contained an acid such as wine or vinegar [27]. The puzzling artifact was dated to the Parthian Empire or the Sasanian Empire, nearly 2000 years old. In 1938, Wilhelm König, director of the National Museum of Iraq, theorized that this artifact was a galvanic cell used for the electroplating of gold or for primitive electrotherapy [28]. It has since been dubbed the Baghdad Battery. Experiments using grape juice and vinegar in an identical setup of iron and copper have yielded modest voltages and the electroplating of gold was reproduced [27]. Though many modern scholars reject the notion that the Baghdad Battery was, in fact, a battery, the idea appeals to humanity's fascination with the past and the unknown [29].

The first battery agreed upon by historians was constructed in 1799, and its seminal discovery provides an introduction into the three components of a battery. Italian physicist Luigi Galvani observed that when a dead frog leg was connected in series with two metals, it would twitch and spasm. He attributed this movement to animal electricity – energy stored within the muscles [30]. Physicist Alessandro Volta impugned Galvani's claims, believing the energy came from the different metals being joined by a moist intermediary. In his efforts to disprove Galvani, he built what is today called the voltaic pile – a stack of alternating copper and zinc disks separated by cloth soaked in brine. When the top and bottom disks were connected by a wire, current would flow between them [31]. Two centuries of research into the optimal materials culminated in Sony's 1991 release of the rechargeable, energy-dense lithium-ion battery. This battery and its progeny shape our world today [32].

I have discussed the motivations for new batteries. I have discussed the history of batteries. Now, finally, I discuss the science of batteries. The aim of research is to answer a question.

In order to ask the right question, one must understand both where society is going and where society has been. What does the world need that science can provide? What have scientists before me discovered and left unanswered? At times, researchers become so entrenched in their work, its applicability vanishes. This leads to the wasteful spending of funds and use of resources. Now that I have answered for myself and for you why we need to research batteries, I am confident in moving on to the science.

1.2.1 Battery Fundamentals

A battery is a device that stores chemical energy and converts it to electrical energy. It is a deliberate configuration of materials which exploits natural laws to serve human ends. A battery consists of two electrodes, the cathode and the anode, separated by an electrolyte. As shown in Figure 1.1, when a battery is discharged, electrons flow from the anode through a circuit to the cathode. Meanwhile, ions flow between the electrodes through the electrolyte to donate or accept these electrons. The discharge process is spontaneous and releases energy. When a rechargeable battery is charged, energy is inserted into the system so the electron and ion flows reverse and the battery can be used again.

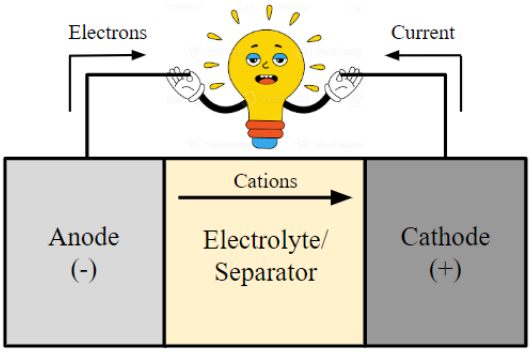

Fig. 1.1 Schematic of a basic electrochemical cell showing ion and electron movement during discharge.

The mechanism in a battery which causes electrons to flow through a circuit is a category of chemical reactions known as reduction-oxidation (redox). A reduction half-reaction occurs when a chemical species gains electrons, thus its overall charge is reduced. An oxidation half-reaction occurs when a chemical species loses electrons; the term was first coined in the 18th century by Antoine Lavoisier to signify reaction with oxygen, but later extended to any reaction involving electron loss. When a battery is charged, an applied electric current enables reduction at the anode and oxidation at the cathode. When a battery is discharged,

natural forces cause reduction at the cathode and oxidation at the anode. These forces are a consequence of a quantity called chemical potential, μ. The chemical potential of an electrode is the energy required to add or remove an electron from the electrode surface when it is in contact with an electrolyte solution. Its value is affected by the electrode material, thus the redox reaction occurring, the electrolyte ion concentration, and the temperature. Any two conducting materials with different chemical potentials can act as electrodes in a battery. The larger the difference in chemical potential between the anode and cathode, the larger the operating voltage, as shown in Figure 1.2.

An electrolyte is a solid, liquid, or gel between the cathode and anode which maintains charge balance in the battery. When electrons flow externally through the circuit, ions flow internally through the electrolyte, accepting electrons at either electrode as outlined in Table 1.1. Liquid electrolytes are commonly soaked into a separator, a porous barrier which conducts ions, improves cell stability, and prevents short circuits. The electrolyte stability window quantifies the range of safe operating potentials for a given electrolyte. Outside of this window, parasitic chemical reactions occur, resulting in gas formation, electrode decomposition, and electrolyte breakdown. These can cause confounding contributions to capacity [33].

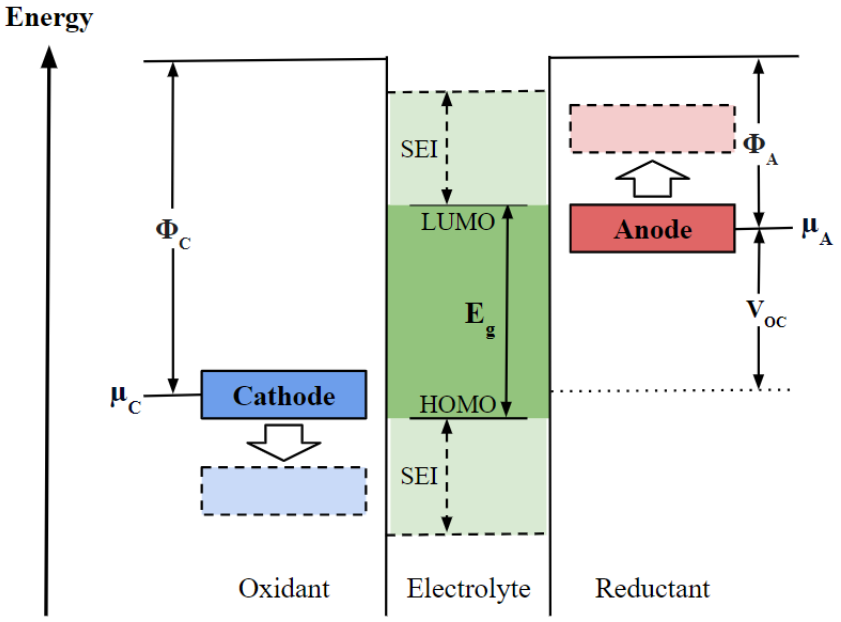

Fig. 1.2 Energy diagram of a cell illustrating the electrolyte stability window, E_g. If the anode chemical potential is above the least unoccupied molecular orbital, $\mu_a > LUMO$, or the cathode chemical potential is below the highest occupied molecular orbital, $\mu_c < HOMO$, a solid-electrolyte interface (SEI) is necessary for a stable system [34].

	Charging	Discharging	
Positive Electrode	Deintercalation	Intercalation	Ionic Process
	Oxidation	Reduction	Electronic Process
Negative Electrode	Intercalation	Deintercalation	Ionic Process
	Reduction	Oxidation	Electronic Process

Table 1.1 Summary of the electron and ion movement at both electrodes during charge and discharge in an intercalation battery. Traditionally, an anode is defined as an electrode undergoing an oxidation reaction, and a cathode is defined as an electrode undergoing a reduction reaction. This means that during charge, the positive electrode is the anode and the negative electrode is the cathode, but during discharge, the positive electrode is the cathode and the negative electrode is the anode. It is convention in battery research, however, to always call the positive electrode the cathode and the negative electrode the anode. This is the standard I will follow.

1.2.2 Measures of Performance

I have defined the main battery components: cathode, anode, and electrolyte, as well as the working principles: redox reactions, electron flow, and ion flow. Next, I detail the measures of performance in a battery: energy, power, and stability. By mathematically defining these properties, batteries can be compared and research can be targeted. The total energy stored in a battery is the integral of its voltage (V) with respect to its capacity (C):

$$E = \int V(C)dC = \int V(t)Idt \tag{1.1}$$

where I is current and t is time. Voltage is the electrochemical potential difference between the anode and cathode. The value of a battery's voltage depends on the materials selected for the electrodes. A useful comparative tool in battery research is the open circuit voltage, V_{oc}, of a fully-charged cell. Open circuit voltage is defined as the potential difference measured across the terminals of a cell when it is neither charging nor discharging

$$V_{oc} = \frac{\mu_A - \mu_C}{e} \tag{1.2}$$

where e is the charge of an electron and μ_A and μ_C are the chemical potentials of the anode and cathode, respectively.

Capacity is the amount of electric charge moved by a battery. A larger battery will evidently hold more charge, thus having a higher capacity, but battery materials can be compared by analyzing charge per unit mass, gravimetric capacity, or charge per unit volume,

volumetric capacity. The theoretical gravimetric capacity, Q, of a chemical compound is calculated using the formula:

$$Q = \frac{1000 \times \Delta x \times F}{3600 \times M_W} \tag{1.3}$$

where the Faraday constant F = 96,485 s·A·mol^{-1}, Δx is the number of electrons transferred per single ion, and M_W is the molecular weight of the electrode. The numerical factors give units of gravimetric capacity, mA·h·g^{-1}. The true capacity of an electrode material is calculated by multiplying the current by the reaction time. This capacity is always less than the theoretical capacity due to design and operation limitations, but theoretical capacity serves as a tool of comparison and an indicator of promising materials.

The second measure of a battery's performance is power. Energy quantifies the amount of work a battery can do, while power quantifies the rate at which that work can be extracted. The power (P) of a battery is defined as:

$$P = IV - I^2 R_{int} \tag{1.4}$$

where I is the current drawn, V is the voltage, and R_{int} is the internal resistance. In electrode research, instead of using the numerical current value of I, the charge rate C/t is used to quantify cycling regimes. The time t is measured in hours, thus $C/50$ would mean the current required to fully charge or discharge a cell with capacity C in 50 hours. Charge rate allows electrodes of differing masses to be compared and also gives insight into power.

Two factors affecting battery power are transport kinetics and phase transitions. It is important to select electrode materials which have optimal electron conductivity and ion diffusion. Conductivity of the electrode assembly is improved by coating cathode crystals in carbon. Ion diffusion is improved by selecting intercalation compounds with diffusion pathways of low activation energy. Some materials, such as $LiFePO_4$, undergo phase transitions during cycling which occur at slow rates. This can hinder rapid (dis)charge [35]. In summary, batteries should be tailored to their uses, but if one desires to maximize power, then materials with good transport kinetics and minimal phase transitions should be selected.

The final measure of performance in a battery is stability. A robust, rechargeable battery should have a long lifetime and operate in different environments. Stability is divided into mechanical, electrochemical, and thermal stability. During cycling, a battery should experience minimal volume change to ensure mechanical stability. As discussed, electrodes and electrolytes must be compatible to avoid degradation over time. Finally, a battery should operate safely under the extreme hot or cold conditions and fast or slow rates demanded by consumers.

1.2.3 Intercalation

Primary batteries are single-use. Secondary batteries are rechargeable. There are three mechanisms by which ions can be reversibly stored in secondary batteries: conversion, alloying, or intercalation reactions. In a conversion reaction, the active material in the electrode undergoes a chemical transformation during charge and discharge. Advantages of conversion reaction batteries include high capacities and inexpensive materials. Disadvantages include parasitic side reactions which degrade performance rate over time. In an alloying reaction, the active material in the electrode forms an alloy, or mixed metal, with the ions from the electrolyte during charge and discharge. Advantages of alloying reaction batteries include high power densities and capacities. A disadvantage is lower cycle life. Alloying materials are prone to expansion and contraction during charge and discharge, which leads to mechanical stress. The dominant method in battery technology is intercalation. Intercalation is the reversible insertion of ions into the lattice structure of a material without significant changes to the host material's crystalline structure. Advantages include high cycle life and good capacity retention, meaning that the battery can be cycled many times without significant degradation in performance. Additionally, intercalation materials often have high energy density. Disadvantages include lower power density compared to other types of battery materials, which means they may not be suitable for applications that require rapid discharge or charging.

Think of intercalation like Hasbro's classic 1974 game: Connect Four. The blue rack is analogous to a host lattice in an electrode, and the holes represent vacancies. The colored game tokens can be thought of as ions. In Connect Four, the tokens naturally fall into place until the rack is full. In batteries, ions from the electrolyte naturally fill host vacancies in the electrode when current is permitted to flow. With this visualization in mind, one can imagine two ways to fill the board: in order or at random. As depicted in Figure 1.3, an ordered occupation of host lattice vacancies by ions is called two-phase intercalation. A random occupation is called solid solution intercalation. The subtle difference in these microscopic processes affects the overall performance of the battery. During two-phase intercalation a moving interface separates the two phases, occupied and unoccupied, within a single electrode particle's lattice. Because the composition of the original material, unoccupied, remains the same during intercalation, the process occurs at a constant voltage. There is an activation energy required to nucleate the reaction front during two-phase intercalation. During solid solution intercalation, the random occupation of sites within the host lattice means that each new ion that encounters the host lattice reacts with different material. This variable composition results in a nonconstant, sloped voltage during (dis)charge.

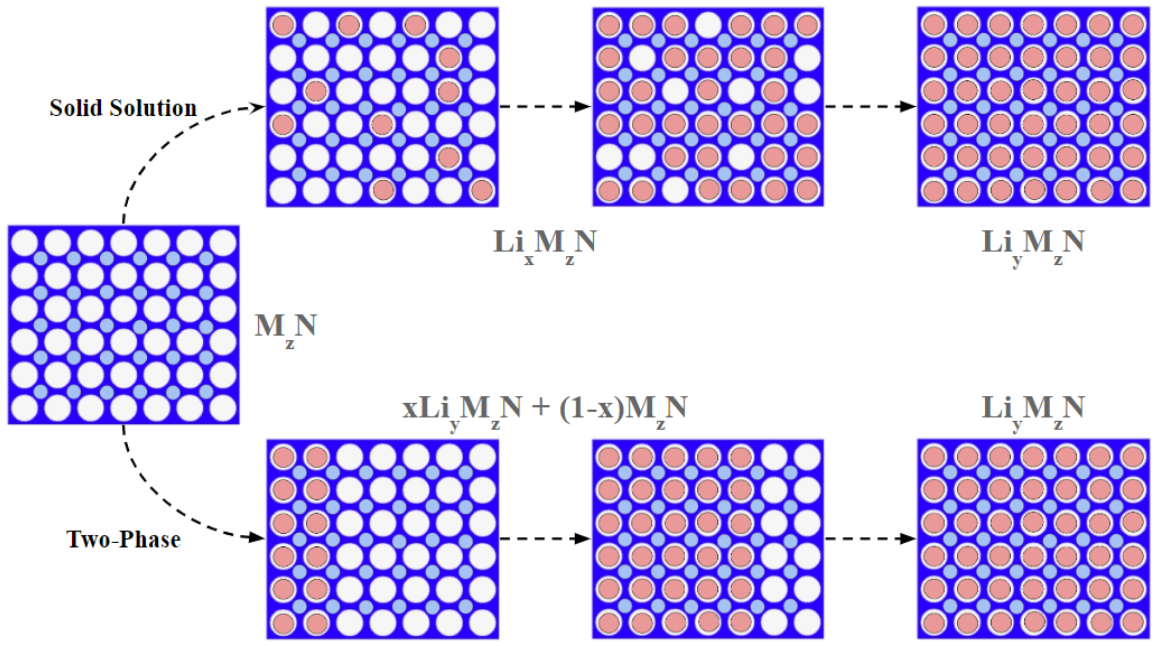

(a)

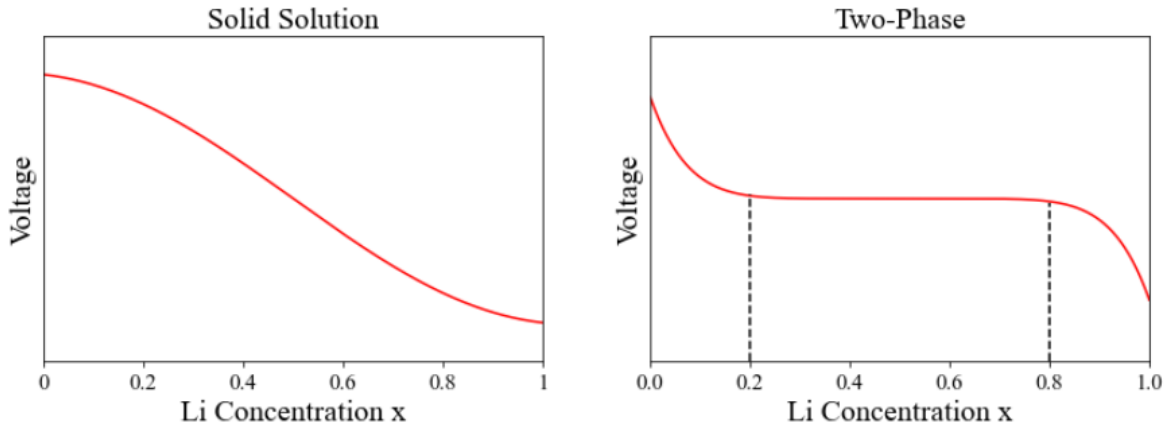

(b)

Fig. 1.3 (a) The two intercalation mechanisms in a lithium-ion cathode and (b) their associated voltage vs. lithium concentration plots.

"Each metal has a certain *power*, which is different from metal to metal, of setting the electric fluid in motion." - Alessandro Volta

1.3 Magnesium-Ion Batteries

The following is a discussion of magnesium-ion batteries and polyanion cathodes. I begin by answering an unaddressed question from section 1.1. It is apparent that there is a growing demand for batteries, but why do we need new batteries when a proven archetype already exists? I respond to this by detailing problems with cost, safety and performance in lithium-ion batteries. I list alternate battery candidates before highlighting the merits of magnesium-ion batteries and polyanion cathodes.

1.3.1 Lithium-Ion Battery Shortcomings

The modern electronics industry is dominated by lithium-ion batteries. The cathodes include lithium cobalt oxide ($LiCoO_2$), lithium iron phosphate ($LiFePO_4$), and members of the spinel family, such as $LiMn_2O_4$. The anodes are lithiated graphite or lithium metal. The electrolyte is some concentration of lithium hexafluorophosphate ($LiPF_6$) in ethylene carbonate/dimethyl carbonate. One cannot overstate the value of this technology. Lithium-ion batteries facilitate portability in the Third Industrial Revolution. Their discovery earned John B. Goodenough, Akira Yoshino, and M. Stanley Whittingham the 2019 Nobel Prize in Chemistry. Lithium-ion batteries have driven and will continue to drive society into the future, but shortcomings in their cost–both financial and ethical, safety, and performance invite research into alternative options.

Lithium is expensive and lithium deposits are only present in certain regions of the world. The price of lithium carbonate (Li_2CO_3), one common mineral used to synthesize lithium cathodes, increased by over 350% from 2017 to 2022 as demand grew. In July 2023, the price slightly dropped to $40,000 per metric ton due to concerns over the lack of EV sales, yet this price is still significantly higher than that of the minerals required to synthesize alternate battery cathodes currently under development [36]. The largest producers of lithium in the world are Australia (53%), Chile (22%), China (10%), and Argentina (8%) [37]. The largest deposit of lithium in the world sits in Afghanistan [38]. Given the dynamics of international relations and the fragility of supply chains exposed by the COVID-19 pandemic, it is desirable to pursue battery technologies composed of more abundant elements.

In transition metal oxides, like $LiCoO_2$, the transition metals provide stability, increase voltage, and facilitate redox reactions during electrochemical cycling. For these reasons, they

are essential to the operation of modern lithium-ion batteries, yet cobalt has a high monetary and ethical price. In July 2023, the cost of cobalt was $42,000 per metric ton compared to $21,000 for nickel, $1000 for iron, and $900 for manganese [36]. Additionally, 70% of the world's cobalt comes from the Democratic Republic of the Congo [39]. The artisanal and small-scale mines in this country harbor human rights abuses including toxic exposure, child labor, and slave labor [40]. Cobalt is also a carcinogen. For these reasons, researchers ought to investigate cathode materials without cobalt as replacements for the $LiCoO_2$ cathode.

In addition to cost and human rights concerns with lithium-ion batteries, there are appreciable safety concerns. The United States Federal Aviation Administration (FAA), the United Kingdom Civil Aviation Authority (CAA), and the European Union Aviation Safety Agency (EASA) all restrict the storage of lithium-ion batteries in the cargo holds of passenger planes and limit the size of those allowed in the cabin. This is because they pose explosion and fire risks. Since the dawn of the social media era, there have been numerous viral videos of lithium-ion battery explosions in electric scooters, vape pens, and EVs [41–43]. What is the cause of these explosions and how can it be addressed? The carbon-based compounds in the electrolyte are flammable and the cathode provides a source of oxygen. An internal short circuit, excessive external heating, overcharging, or physical damage to a battery can provide the impetus for combustion. One problem for lithium-ion batteries, particularly those with lithium metal anodes, is dendrite formation. Dendrites are sharp, tree-like formations composed of lithium. They grow from the anode toward the cathode as lithium is repeatedly deposited and dissolved during cycling. Eventually, they pierce the separator and reach the cathode causing an internal short circuit and possible combustion. An array of methods to mitigate dangers in lithium-ion batteries have been researched and implemented, yet it is a rational decision to pursue new technologies which eliminate these risks [44].

The final shortcoming in lithium-ion batteries is performance. While the single-charge capacity and cycle lifetime of lithium-ion batteries are exceptional relative to historical standards, the consumer demands more. In cellphones, laptops, and other electronics, the battery is consistently the first point of failure. Continued research on lithium-ion batteries will result in incremental improvements, but there is a fundamental limit on the energy within the element. Scientists ought to research novel materials and chemistries in order to dramatically improve battery performance.

1.3.2 Magnesium-Ion Battery Merits

In response to the lithium-ion battery shortcomings enumerated above, scientists are investigating rechargeable metal-ion batteries composed of sodium, potassium, magnesium, zinc, aluminum, and others (Table 1.2) [45–47]. Additionally, there is research being done on

novel electrochemistries, such as metal-air and redox flow batteries [48, 49]. This thesis will focus on magnesium-ion batteries.

Primary magnesium batteries have existed since the early 20th century, but have found limited commercial success. They have been used in multiple military applications as dry cells. In a dry cell, the electrolyte, often salt water, is added only when the battery is ready to be used, offering an indefinite shelf life. The BA-4386 magnesium dry battery was used by the US military from 1968-1984 to power radios during the Vietnam War because it offered a superior volumetric capacity to contemporary zinc batteries [50]. The Mark 44 anti-submarine torpedo, operated by the Americans, British, Canadians, and Australians from 1957-1967, was powered by a seawater-activated battery with magnesium and silver chloride electrodes [51]. In recent years, attention has returned to magnesium as a possible secondary battery after researchers demonstrated the intercalation of magnesium in the chevrel phase, Mo_3S_4, in 2000 [52]. The quest for a cathode material with high capacity, high voltage, and competitive stability remains.

Property	Li	Na	K	Mg	Ca	Zn	Al
Valence	+1	+1	+1	+2	+2	+2	+3
Cationic Radius (Å)	0.76	1.02	1.38	0.72	1.00	0.74	0.54
Atomic Weight (g/mol)	6.94	22.990	39.098	24.305	40.078	65.380	26.982
E (V vs. SHE)	-3.04	-2.71	-2.93	-2.37	-2.87	-2.20	-1.66
Metallic Capacity (mAh/g)	3862	1166	685	2205	1337	820	2980
Metallic Capacity (mAh/cm^3)	2062	1128	591	3833	2073	5854	8046

Table 1.2 Comparison of the physical and electrochemical properties of prospective metal-ion batteries with lithium [35]. The energy is expressed in volts vs. the standard hydrogen electrode (SHE), a reference electrode used in electrochemical measurements, serving as the zero point for electrode potentials

A rechargeable magnesium-ion battery holds the following advantages over lithium. Concerning cost, magnesium is over 1000 times more abundant than lithium in the Earth's crust by weight (2.08% vs. 0.0017%) [53]. The price of the raw mineral containing magnesium is 20 times less than that of lithium ($2000 per metric ton vs. $40,000 per metric ton) [36]. Additionally, it is conceivable to use transition metals other than cobalt in a functional magnesium-ion battery avoiding further cost and ethical concerns. Concerning safety, although they have been reported, research shows that under normal operating current densities dendrites do not form in magnesium-ion batteries, so a magnesium metal anode

could be used, further increasing energy density [54, 55]. Finally concerning performance, the magnesium ion (Mg^{2+}) is divalent meaning for the movement of a single ion, it carries twice the charge of a lithium ion (Li^{+}). Additionally, the volumetric capacity of magnesium is nearly twice that of lithium.

Given these advantages, what's the hold-up? The divalency of the the magnesium ion, though in one regard a benefit, hampers intercalation within the cathode and diffusion in the electrolyte. Its larger electric charge causes it to become trapped in defects and interact more strongly with electrolyte species [56]. Additionally, research has not identified a suitable electrolyte. There is a tendency for a insulating surface layer to form over magnesium metal anodes as a result of electrolyte decomposition which prevents further cycling. Electrolytes which do not exhibit this behavior have had unsatisfactory stability windows [57]. In summary, a high-performance, commercially-viable rechargeable magnesium-ion battery is conceivable, but the elusive cathode and electrolyte have befuddled researchers.

1.3.3 Polyanion Cathodes

One avenue of research for a magnesium-ion battery cathode is the family of polyanion materials. In the field of lithium-ion batteries, host frameworks composed of transition metals bonded with (XO_a) groups, where X = B, P, S, Si, have shown improved safety, cycle life, and voltage over oxide frameworks [58]. The strong covalent bonds in the polyanion group reduce the likelihood of O_2 formation and thermal runaway. The robust nature of the polyanion groups minimizes volume change during cycling, increasing longevity. Finally, the inductive effect allows for higher operating potentials for the same transition metal redox couple.

The inductive effect is a consequence of the higher electronegativities of polyanions. Bringing multiple oxygen atoms and a nonmetal together improves their electron-withdrawing ability. Polyanions have a higher tendency to form sigma bonds with the transition metals in the cathode. Lone electron pairs overlap with the vacant orbitals of the transition metals head-on along the internuclear axis. In oxide frameworks, there is a higher tendency to form π-bonds between the oxygen atoms and the transition metals. In a π-bond, p orbitals overlap above and below the internuclear axis resulting in a weaker bond. This means that in a polyanion cathode, the inductive effect will stabilize higher oxidation states, thus allowing for higher operating voltages as shown in the example in Figure 1.4.

One obstacle in polyanion cathodes is limited rate performance caused by poor electrical conductivity. The strong covalent bonds between the anions inhibit electron flow. This is the limiting factor on high rates of ion intercalation.

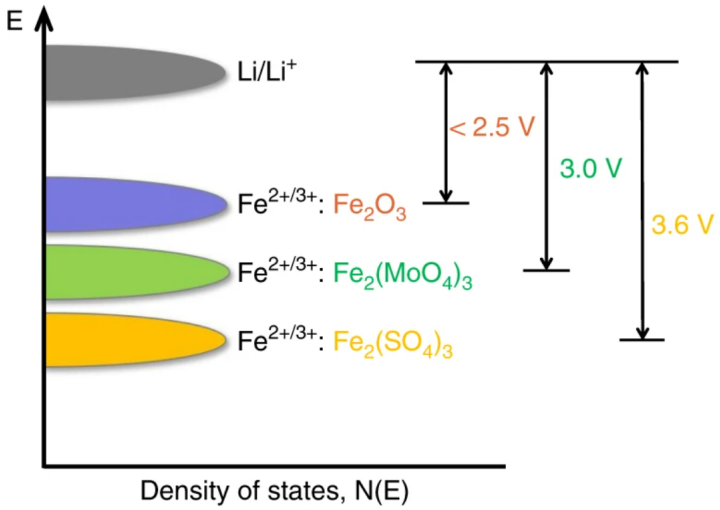

Fig. 1.4 Energy diagram showing the lowering of the redox energies of the $Fe^{2+/3+}$ couple and the consequent increase in cell voltage from a simple oxide, Fe_2O_3, to different polyanion oxides, $Fe_2(MO_4)_3$ and $Fe_2(SO_4)_3$, with varying electronegativities [59]

"Make the best use of what is in your *power*, and take the rest as it happens." - Epictetus

1.4 Thesis Overview

In this section, I outline my project goal: investigating orthoborates, $Mg_2M(BO_3)_2$, where M=Mn, Ni, as high capacity and high voltage magnesium-ion intercalation cathode materials. I also synthesized $LiFeBO_3$ to verify my experimental method with a known material and investigate the affects of different carbon additives.

The borate group, $(BO_3)^{3-}$, exists in a trigonal-planar arrangement. It is the lightest of the polyanion groups, so it exhibits the inductive effect while maximizing capacity. Lithium metal borates, $LiMBO_3$, shown in Figure 1.5, have been studied extensively [60]. They exhibit high voltages (>4 V) and high capacities (>200 $mA{\cdot}h{\cdot}g^{-1}$) depending on the transition metal present, but often exhibit capacity fade over repeated cycling. They most commonly exist in the monoclinic (*C 1 2/c 1*) crystal structure which has clear lithium intercalation columns along the [001] direction. MO_5 trigonal bipyramids are edge-shared along [101] direction allowing electronic transport, while LiO_5 polyhedra are edge-shared along [001] direction. Super P and Ketjenblack are two popular carbon powders which are mixed with cathode crystals to increase electrical conductivity. Ketjenblack has a higher surface area than Super P, but also a higher price. In this thesis, I investigate how the choice of carbon additive in the cathode affects the electrochemical performance of $LiFeBO_3$.

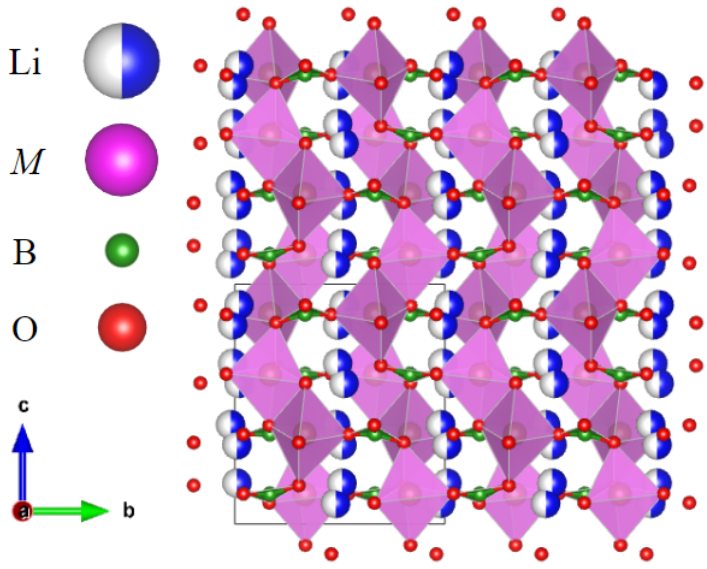

Fig. 1.5 Crystallographic structure of monoclinic $LiMBO_3$ shown along the [100] axis illustrating the Li-ion intercalation channels. *Created using VESTA* [61].

Magnesium orthoborates, $Mg_2M(BO_3)_2$, shown in Figure 1.6, have an orthorhombic (*Pnnm*) crystal structure with layers of trigonal-planar $(BO_3)^{3-}$ groups. There are two distorted octohedral metal sites, $M1$ and $M2$. The sites are randomly occupied by magnesium and the transition metals. Bond valence sum calculations show that an intercalation pathway exists for magnesium, meaning that removal of the Mg ions does not result in an unfavorable energy configuration in the crystal lattice [62]. Using equation 1.3, the theoretical capacities of $Mg_2Mn(BO_3)_2$ and $Mg_2Ni(BO_3)_2$ are 242.3 mAh/g and 238.3 mAh/g respectively, making them promising cathode materials. Naturally-occurring orthoborates were discovered in the late 17th century. Mixed-metal orthoborates were first synthesized and characterized in the late 20th century [63]. Orthoborates as cathode materials for magnesium-ion batteries were not proposed until 2017 by Hugh Glass [62]. This thesis builds on his work. I reproduced the synthesis and electrochemistry of $Mg_2Mn(BO_3)_2$. I tested, for the first time, the electrochemical properties of $Mg_2Ni(BO_3)_2$. I performed an array of tests and experiments designed to elucidate the mechanisms responsible for the observed capacities in both materials.

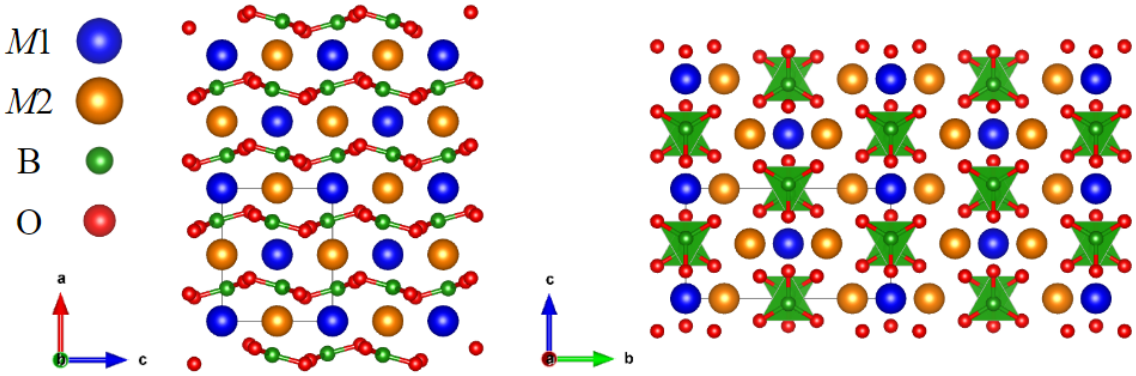

Fig. 1.6 Crystallographic structure of $M_3(BO_3)_2$ shown along the [010] and [100] axes. *Created using VESTA* [61].

Chapter 2

Experimental Techniques

"I love *power*. But it is as an artist that I love it. I love it as a musician loves his violin, to draw out its sounds and chords and harmonies." - Napoleon Bonaparte

2.1 Solid State Synthesis

Before one can test the viability of these materials as battery cathodes, one must make the materials. All cathode crystals were produced via solid state synthesis. Solid state synthesis, also called ceramic synthesis, is a method of creating materials in which chemical reactions occur via solid state diffusion, not involving solvents or liquid phases. Powdered reactants were mixed and heated to high temperatures so that cations and anions freely migrated until the intended crystal product was formed. This method was selected because reactant mass, reactant choice, temperature, and atmosphere could each be separately adjusted to achieve the desired product. Powdered reactants were weighed in stoichiometric amounts and hand-ground with a mortar and pestle or mechanically ball-milled before being pressed into a pellet. This maximized contact and minimized ion diffusion distance. Different reactants containing the same cation were iterated through to find that which minimized impurity formation. Heating occurred in a resistance tube furnace. Multiple heating steps under a controlled atmosphere were necessary to stabilize the correct phase and the desired oxidation states.

Both the magnesium orthoborates ($Mg_2M(BO_3)_2$) and the lithium borates ($LiMBO_3$) were very sensitive to reaction conditions. In the orthoborates, magnesium oxide (MgO) or magnesium acetate ($Mg(C_2H_3O_2)_2$) provided the magnesium, metal oxalates (MC_2O_4) provided the transition metals with 2+ oxidation states, and boric acid (H_3BO_3) provided the polyanion. In the lithium borates, lithium hydroxide (LiOH) or lithium carbonate (Li_2CO_3) provided the lithium, metal carbonates (MCO_3) provided the transition metals with 2+

oxidation states, and boric acid (H_3BO_3) provided the polyanion. Manufacturers can be found in Appendix A. The ground and pelletized mixtures were placed in alumina crucibles and slowly heated ($\leq$ 3°C/min) to high temperatures. As shown in Figure 2.1, multiple heating steps and repeated grinding were necessary, meaning syntheses took up to one week to complete. When inert conditions were required, the heating took place under argon flow and the crucible was wrapped in copper foil to minimize reaction with trace amounts of oxygen.

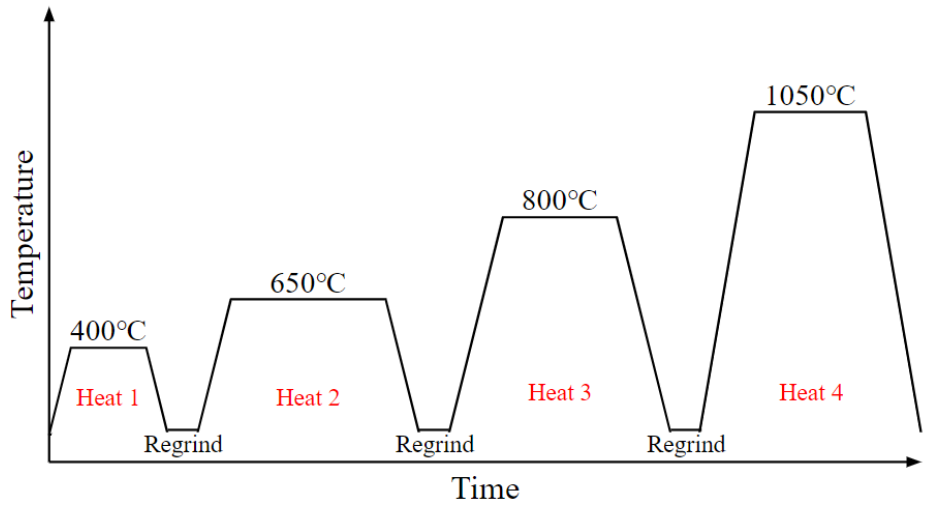

Fig. 2.1 A typical magnesium orthoborate solid state synthesis procedure. The first heat removes carbon and hydrogen from the product as gaseous CO_2 and H_2O. The subsequent heats and grinds increase crystallization and homogeneity. Specific synthesis procedures are outlined in Chapter 3

"Immense *power* is acquired by assuring yourself in your secret reveries that you were born to control affairs." - Andrew Carnegie

2.2 Material Characterization

After the synthesis of each cathode material, powder X-ray diffraction (XRD) and Rietveld refinement were used to characterize the crystal structure and identify impurities [64].

2.2.1 X-Ray Diffraction

In 1912, during his first year at the University of Cambridge, Lawrence Bragg had the insight that if a crystal was composed of parallel atomic planes, then incident X-rays would diffract constructively when the distance travelled between the atomic planes was equal to the wavelength of the X-rays. From this, he crafted the Bragg equation which relates wavelength, atomic layer spacing, and incident angle. In 1914, Bragg commissioned as a second lieutenant in the Leicestershire Royal Horse Artillery serving the entire duration of World War I. In 1915, he won the Nobel Prize in Physics for his discovery [65]. To this day, Bragg's law is widely used to identify crystals from the characteristic X-ray peaks they deflect at certain angles of incidence:

$$n\lambda = 2dsin\theta \tag{2.1}$$

where n is a natural number (the diffraction order), d is the distance between atomic planes, and θ is the angle between the X-ray and the atomic plane.

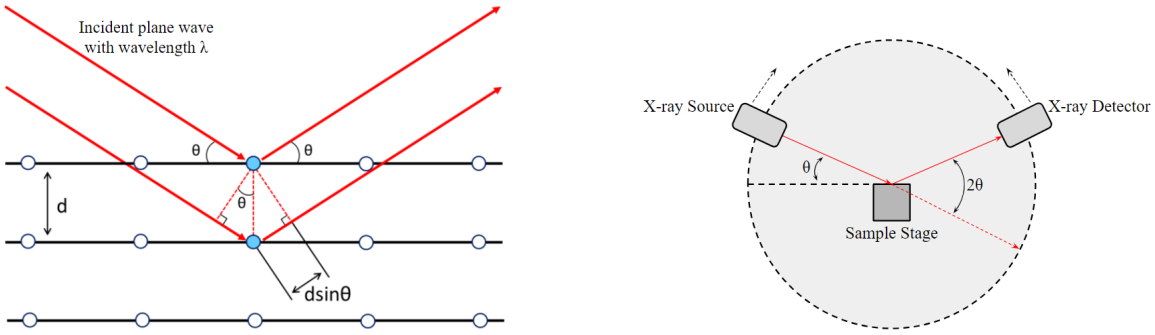

(a) (b)

Fig. 2.2 (a) A depiction of Bragg's Law (b) A schematic of a powder x-ray diffraction device.

As shown in Figure 2.2, an X-ray which elastically scatters off of an atom in one crystal plane will travel a distance $2dsin\theta$ further than an X-ray which scatters off of an atom in the

plane above it. If this distance is equal to an integer multiple of the X-ray wavelength, then constructive interference will occur, resulting in a strong peak in the X-rays detected along the path of reflection. A powder XRD spectrum is the measurement of X-ray intensity as a function of 2θ. Different crystals have unique structures which means that XRD spectra give information about atomic positions, lattice parameters, and phase purity. Cathode samples were finely ground (< 20 nm) and rotated when XRD was performed to ensure random crystal plane orientations, enabling measurement of all potential diffraction directions.

There are two ways to generate the monochromatic X-rays required for XRD: striking a metal target with electrons or accelerating fast-moving electrons in a magnetic field. In the first process, electrons emitted from a heated filament are accelerated toward a metal anode with an applied electric field. When they strike metal atoms, electrons will be ejected from the core shell and outer shell electrons will drop to fill the vacancies. This produces characteristic X-rays with an energy equivalent to the difference between the two shells. Filters are used to select one of these X-ray wavelengths. In this experiment, powder XRD was performed on all cathode crystals using the Bruker D8 Discover. This machine provided rapid, in-house spectra, scanning between $2\theta = 10^\circ$ to 80° over two hours. The instrument used a copper anode where Cu-Kα = 1.54060 Å. The second method relies on synchrotron radiation. When near-light-speed electrons from a particle accelerator are undulated, they release X-rays. This high-intensity, collimated light produces clearer XRD spectra, collecting scans from $2\theta = 2^\circ$ to 90° in 60 seconds with a wavelength of 0.493168 Å. The synchrotron data presented in this thesis were gathered at the Ill diffractometer at Diamond Light Source, Oxfordshire.

2.2.2 Rietveld Refinement

The Rietveld refinement technique utilizes a least squares approach to adjust a theoretical line profile (derived from a known or postulated crystal structure) to align with the measured XRD profile. In 1964, Hugo Rietveld earned his PhD in physics from the University of Western Australia studying crystallography. He continued his work in the Netherlands, and by 1969, he devised and published his eponymous technique [66]. Rietveld refinement was a major breakthrough in crystallography because it simultaneously fit the full XRD profile instead of individual reflections. It informs the user on unit cell dimensions, atomic positions, thermal vibrations, and purity percentages. It works as follows.

First, establish peak positions. They can be calculated using Bragg's law with the instrument wavelength and the postulated d-spacing as determined from the model structure unit cell. Second, determine the peak intensities. The intensities are proportional to the

square of the structure factor, F_{hkl}, which quantifies how an atom will scatter incoming radiation as a function of position and scattering factor.

$$F_{hkl} = \sum_{j}^{N} f_j(\theta) e^{-2\pi i(hx_j + ky_j + lz_j)} \tag{2.2}$$

where N is the number of atoms in the unit cell, x_j, y_j, z_j are the positional coordinates of the j^{th} atom with Miller indices hkl, and $f_j(\theta)$ is the scattering factor of the j^{th} atom. The scattering factor depends on the type of radiation and the species of atom. Third, establish the shape of each peak. The peak shape follows a Voigt function of instrument parameters and sample characteristics. In practice, a pseudo-Voigt function (a linear combination of Gaussian and Lorentzian functions) is used to avoid the computational complexity of convolutions [67]. Fourth, sum the peak functions with the background function to create the resultant XRD profile. A high-order Chebyshev polynomial is selected for the background because it minimizes oscillation across the domain and divergence at the endpoints. Finally, iterate through crystal cell parameters until the theoretical profile matches the experimental spectrum.

The function which is minimized in the iteration process is:

$$\Phi = \sum_{i=1}^{n} w_i (Y_i^{obs} - Y_i^{calc})^2 \tag{2.3}$$

where n is the number of data points, w_i is the weight of the i^{th} data point (proportional to the square root of intensity), Y_i^{obs} is the observed intensity, and Y_i^{calc} is the fitted intensity. The fitted intensity is defined as:

$$Y_i^{calc} = b_i + \sum_{l=1}^{p} K_l \sum_{j=1}^{m} I_{l,j} F_{l,j}(x_i) \tag{2.4}$$

where b_i is the background, p is the number of crystal phases present, K_l is the scale factor of each phase (dependent on weight percent), m is the number of peaks, $I_{l,j}$ is the peak intensity, and $F_{l,j}(x_i)$ is the structure factor.

Goodness of fit is commonly evaluated using the weighted residual profile, R_{wp}.

$$R_{wp} = \left(\sum_{i}^{n} \frac{w_i (Y_i^{obs} - Y_i^{calc})^2}{\sum_i^n w_i (Y_i^{obs})^2} \right)^{\frac{1}{2}} \times 100\% \tag{2.5}$$

All Rietveld refinements were performed using the program TOPAS version 5 [68].

2.2.3 Infrared Spectroscopy

An infrared (IR) spectrometer passes IR light through a sample and measures the amount of energy absorbed at different frequencies. When the frequency of the radiation matches the vibrational frequency of a specific bond in a molecule, energy is absorbed. Different types of chemical bonds and functional groups absorb energy at characteristic frequencies. Impurities can alter the vibrational behavior of a molecule and lead to the appearance of new peaks or shifts in existing peaks in the IR spectrum. By comparing the spectrum of a pure sample with that of a sample containing impurities, differences can be identified.

In this experiment, IR spectroscopy was performed on cathode samples before and after ball milling to probe for changes in bond structures and the introduction of impurities.

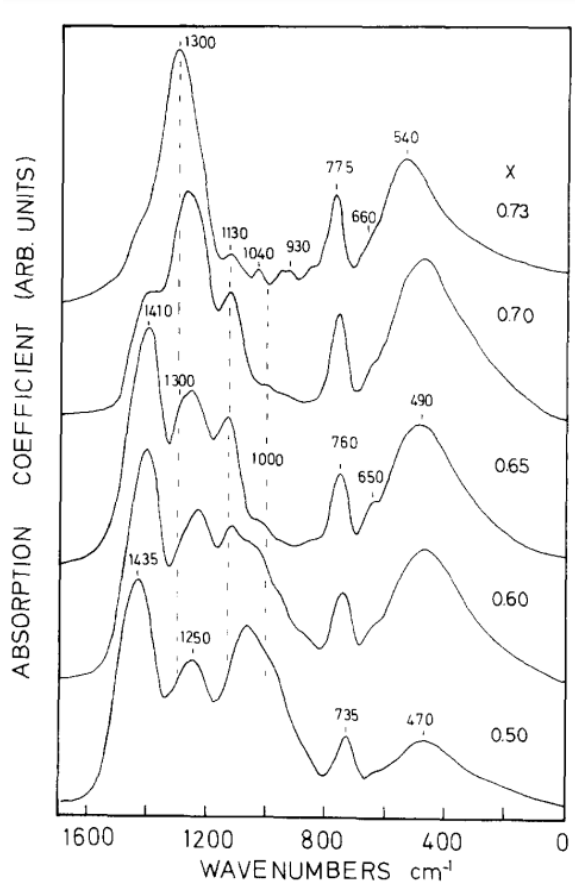

Fig. 2.3 An example of IR absorption spectra collected on lithium borate glasses ($xLi_2O\cdot(1-x)B_2O_3$ [69]

"The problem of *power* is how to achieve its responsible use rather than its irresponsible and indulgent use; of how to get men of *power* to live for the public rather than off the public." - John F. Kennedy

2.3 Cell Construction and Cycling

After synthesizing the cathode materials and confirming their structure and phase purity, CR2032 coin cells were constructed to measure electrochemical performance. Immediately after synthesis, all cathode materials were stored in an Ar atmosphere for cell assembly, cell cycling, and post-cycling analysis to minimize contamination and degradation.

Cathodes were prepared by grinding the borates using a mortar and pestle for 10 minutes with carbon black and polyvinylidene fluoride (PVDF) in a 60:30:10 mass ratio. Carbon ensured the non-conductive active material was electrically connected with itself and the current collector. Ketjenblack was used in all magnesium orthoborates. Super P or Ketjenblack were used in the lithium borates. PVDF binder was used for its thermal and electrochemical stability. Each cell used 5-6 mg of powder placed on the coin cell base as shown in Figure 2.4. Cell guard was placed on the cathode to allow for easy post-cycling analysis. A fiberglass separator was soaked in 12 drops of LP30 electrolyte (1 mol/L LiPF6 in 1:1 ethylene carbonate and dimethyl carbonate). The anode was lithium metal. A Belleville spring provided the necessary pressure in the cell. The spacers, spring, and casings were grade 316 stainless steel.

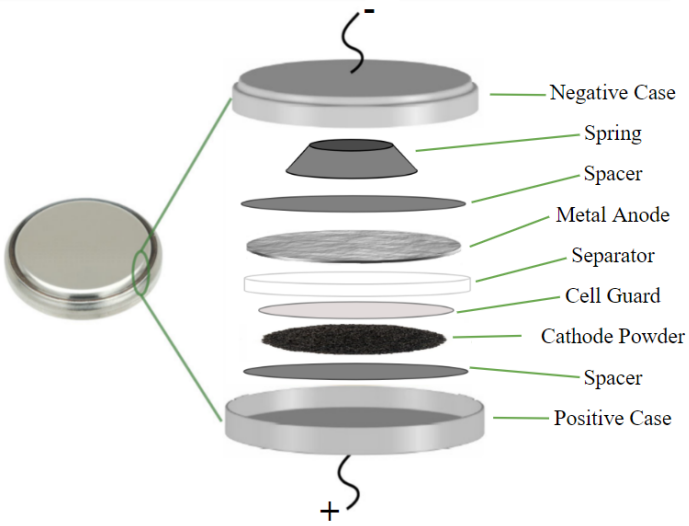

Fig. 2.4 The standard coin cell construction technique used in this experiment

The reason a magnesium-based cathode material was cycled vs. a lithium anode is because effective, commercially-available electrolytes do not exist for magnesium-ion batteries. If cells were prepared using a magnesium metal anode and experimental electrolytes, such as $Mg(TFSI)_2$ in solution, electrochemical performance could not be solely attributed to the cathode. The proven compatibility of LP30 and lithium metal provided a stable environment to assess the electrochemistry of the cathode during first charge. Ideally, in this configuration, magnesium deintercalates on charge and lithium intercalates on discharge.

Cathode materials were assessed with galvanostatic cycling on a Landt CT3001A device. Galvanostatic cycling is the application of a constant current through the coin cell while voltage and capacity are recorded. After construction, cells were rested for 6 hours while V_{OC} was measured. Then, the cells were charged to a set upper voltage limit at which point the current was reversed and they were discharged to a set lower voltage limit. The charge rates used in this experiment were C/20 or C/50. The temperatures used in this experiment were room temperature (20°C) or a constant oven temperature (55°C). The low current and high temperature were selected to allow time for the notoriously slow Mg ion to diffuse.

"In order to obtain and hold *power*, a man must love it." - Leo Tolstoy

2.4 Post-Cycling Material Characterization

Following electrochemical cycling, coin cells were opened in an argon atmosphere for post-cycling analysis. The cathode powder was isolated and washed three times for 5 minutes in 3 mL of dimethyl carbonate to remove residual electrolyte. It was then dried under vacuum for 30 minutes. A battery of tests were performed to investigate changes in material composition and oxidation state during cycling as evidence for or against magnesium deintercalation. These included ex situ XRD, SEM-EDX, SQUID magnetometry, and operando XANES spectroscopy.

2.4.1 SEM-EDX Analysis

The scanning electron microscope (SEM) was invented in 1937 by German physicist Manfred von Ardenne who later went on to play a vital role in the Soviet atomic bomb project [70]. The first commercial SEM was sold by the Cambridge Scientific Instrument Company in 1965 [71]. An SEM produces a high-resolution image of a sample by scanning its surface with a focused beam of electrons. These electrons interact with the sample in different fashions, as shown in Figure 2.5, with each form of radiation giving different information. With a Tescan MIRA3 SEM, secondary electrons were used to image cathode samples and measure particle size. Characteristic X-rays were used to measure elemental composition.

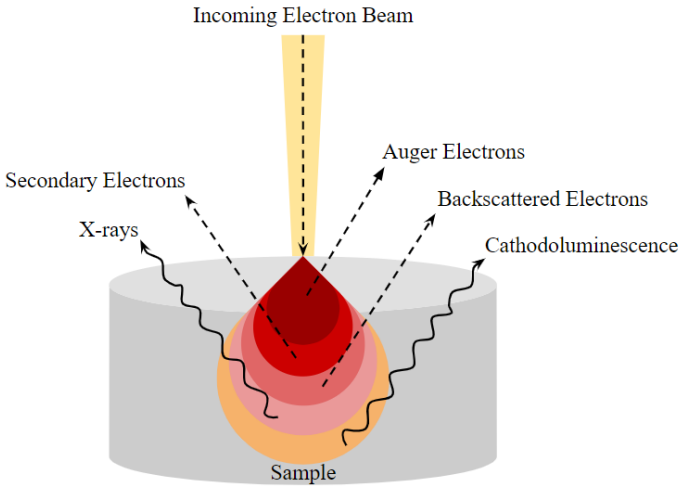

Fig. 2.5 Schematic of a scanning electron microscope illustrating the different types of information-containing emitted radiation.

Secondary electrons are ejected from valence shells in the sample by inelastic scattering with the incoming electron. An Everhart–Thornley detector collects these low-energy electrons, and based on their number and energy, produces a topographical map of a sample's surface. The measurement of X-rays emitted from a sample is called energy dispersive x-ray spectroscopy (EDX). Sometimes, incoming electrons will excite inner shell electrons to a higher energy level. When an electron naturally relaxes to fill the vacancy, a photon will be emitted with an energy equal to the difference in electron levels. Different species of atoms emit unique X-ray wavelengths which can be measured with a silicon drift detector and matched to a database of known atoms. In this experiment, EDX was performed on cathode samples in the pristine and charged states to investigate how the atomic ratio of magnesium changed with respect to the transition metal present. This ratio should vary in an intercalation cathode. The boron and oxygen atomic ratios were not used because they are lighter elements, thus they emit wavelengths which overlap with the signal from the heavier metals.

2.4.2 SQUID Magnetometry

A superconducting quantum interference device (SQUID) magnetometer measures extremely weak magnetic fields. For this reason it is a valuable tool to detect changes in the oxidation states of paramagnetic atoms using the Curie-Weiss law. During charging, when the working ion is deintercalated from the cathode, the transition metals will oxidize to maintain charge balance. Paramagnetic atoms, such as manganese and nickel, have unpaired electrons which generate a magnetic moment. When these atoms change oxidation state, the magnetic behavior will perceptibly change. This means that magnetic measurements performed on the cathode before and after charging can support or undermine the argument that deintercalation is taking place.

The Curie-Weiss law describes the relationship between the magnetic susceptibility of a paramagnetic material and its temperature. It is expressed as follows:

$$\chi = \frac{C}{T - \theta_{CW}} \tag{2.6}$$

where χ is the molar susceptibility, C is the Curie constant (a material property), T is the temperature in Kelvin, and θ_{CW} is the Curie Temperature (the temperature at which thermal and magnetic interactions are equal).

A Quantum Design magnetic property measurement system (MPMS) 3 was used to measure the magnetization of cathode samples from 10-400 K. Magnetization was converted to molar susceptibility via the relationship:

$$\chi_{mol}[emu \cdot mol_N^{-1} \cdot Oe^{-1}] = \frac{M[emu]}{H[Oe]} \frac{M[g \cdot mol^{-1}]}{m[g] \cdot n} \tag{2.7}$$

where the units of each quantity are expressed in brackets. χ is the molar susceptibility, M is the magnetization and molar mass, H is the applied magnetic field, m is the sample mass, and n is the number of magnetic ions per formula unit. A linear least squares regression was fit to inverse molar susceptibility vs. temperature data like that in Figure 2.6. The coefficients were used to calculate the Curie constant and Curie temperature. The Curie constant relates to the average magnetic moment per ion, μ_{av}, in the following relationship:

$$C = \frac{1}{8}\mu_{av}^2. \tag{2.8}$$

The calculated value for the average magnetic moment was compared to the known effective magnetic moments of the transition metal present to determine its oxidation state. Effective magnetic moments are calculated using the following formula which assumes only spin contributions:

$$\mu_{eff} = g\sqrt{S(S+1)}\mu_B \tag{2.9}$$

where $g \approx 2.0023$ is the spectroscopic splitting factor, S is the spin quantum number, and μ_B is the Bohr magneton.

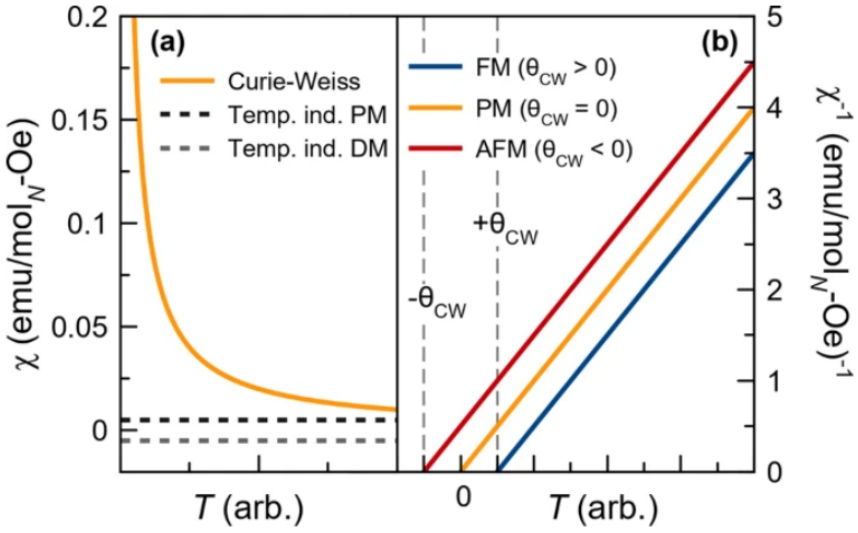

Fig. 2.6 Curie-Weiss behavior in susceptibility and inverse susceptibility [72]

2.4.3 XANES Spectroscopy

X-ray absorption spectroscopy (XAS) is used to determine the local geometric and electronic structure of matter. A sample is irradiated with a beam of synchrotron X-rays whose energy is varied while absorption is measured. As the energy increases, there is a spike at the absorption edge of the probed element. The energy of the absorbed X-rays corresponds to the energy difference between the core and valence electron levels of the atom. There are two types of analysis to perform on XAS spectra: X-ray absorption near-edge structure (XANES) and extended X-ray absorption fine structure (EXAFS). During XANES spectroscopy, researchers analyze the pre-edge and rising edge of spectra to learn about oxidation state, coordination environment, and electronic transitions. Different oxidation states have different valence electron energy levels. As the oxidation state of an atom changes, the absorption edge position detectably shifts as seen in Figure 2.7. During EXAFS spectroscopy, researchers analyze the oscillatory behavior of the absorption coefficient beyond the absorption edge to learn about coordination distances and coordination numbers. These oscillations arise from the interference of X-rays scattered by neighboring atoms around the absorbing atom.

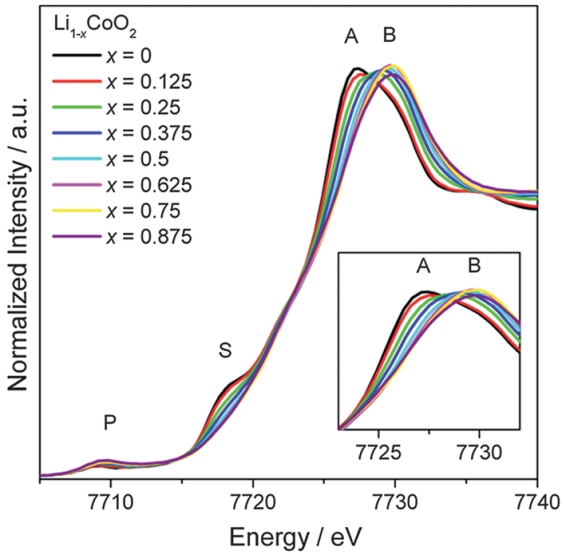

Fig. 2.7 Experimental example of changes in the Co K-edge XANES spectra of $LiCoO_2$ at various states of charge [73]

Operando XANES experiments were performed in B18 at Diamond Light Source, Oxfordshire. Electrochemical cells were prepared in an argon atmosphere by stacking the cathode, separator, and anode in a special case with beryllium windows. This assembly allowed XANES analysis to be performed on the transition metal present in the cathode while cells actively cycled.

Chapter 3

Results

"The measure of a man is what he does with *power*." - Plato

3.1 $Mg_2Mn(BO_3)_2$ and $Mg_2Ni(BO_3)_2$

3.1.1 Synthesis

$Mg_2M(BO_3)_2$ were synthesized from MgO, $MnC_2O_4 \cdot 1.75H_2O$ or $NiC_2O_4 \cdot 2H_2O$, and H_3BO_3 in a 2:1:2 molar ratio. The procedures are detailed in Table 3.1.

	Step	Ramp Rate (°C/min)	Temperature (°C)	Time (hr)
$Mg_2Mn(BO_3)_2$	1	3	400	10
	2	3	650	24
	3	3	800	24
	4	1	1050	24
$Mg_2Ni(BO_3)_2$	1	3	400	10
	2	3	650	24
	3	3	800	24
	4	3	1050	24

Table 3.1 Successful $Mg_2M(BO_3)_2$ synthesis procedures. $Mg_2Mn(BO_3)_2$ occurred in Ar; $Mg_2Ni(BO_3)_2$ occurred in air.

The MgO was preheated to 700°C (at 5 °C/min) for 20 hrs and weighed at 250°C to decompose magnesium carbonate. Before step 1, the powdered reactants were ground for 10 minutes with a mortar and pestle and pressed into a 13 mm diameter pellet. Between each step, the sample was cooled naturally, reground, and pelletized. The $Mg_2Mn(BO_3)_2$ pellet was placed in an alumina crucible wrapped in copper foil and heated in a tube furnace with

flowing Ar gas. Additional copper foil was placed up-flow of the crucible to react with any trace oxygen, thus stabilizing the Mn^{2+} oxidation state. The $Mg_2Ni(BO_3)_2$ pellet was placed in an alumina crucible and heated in air. Phase pure $Mg_2Mn(BO_3)_2$ is white and phase pure $Mg_2Ni(BO_3)_2$ is bright green.

3.1.2 Material Characterization

Crystal Structure

Rietveld analysis was performed on the Ill synchrotron data for both samples. Each crystal site was constrained to be fully occupied, but the Mg:*M* ratio was not constrained to be 2:1. The powder XRD spectra (Figure 3.1) and refined crystal parameters (Table 3.2) reveal the similarities between $Mg_2Mn(BO_3)_2$ and $Mg_2Ni(BO_3)_2$. Differences of note which may affect electrochemical performance include the unit cell volume and the site occupancies. The manganese-containing orthoborate has a cell volume of 213.26(2) $Å^3$, while the nickel-containing orthoborate has a smaller cell volume of 203.268(5) $Å^3$. In $Mg_2Mn(BO_3)_2$, magnesium is the dominant metal at both crystal sites with an 82:18 and 60:40 ratio to manganese at *M*1 and *M*2. In $Mg_2Ni(BO_3)_2$, magnesium is only dominant at the *M*2 site with a 27:73 and 90:10 ratio to nickel at *M*1 and *M*2. The preferential occupation of the higher symmetry, *M*1 site by nickel is possibly attributed its directional *d* orbitals.

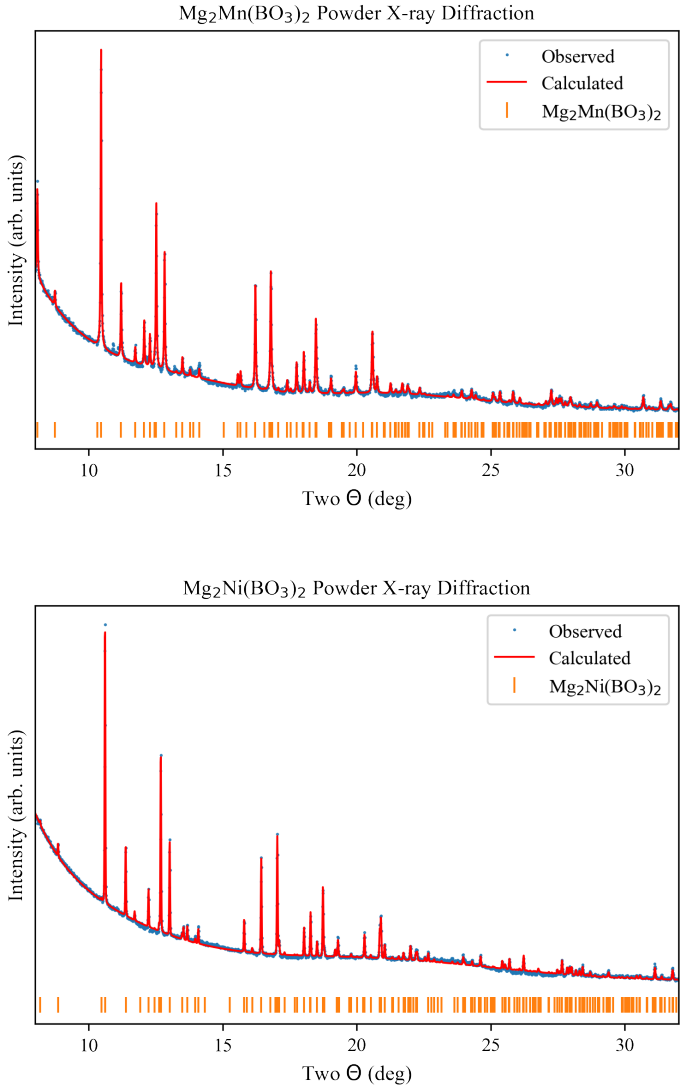

Fig. 3.1 Synchrotron XRD (blue) of the orthoborates collected with $\lambda = 0.493168$ Å, Rietveld refinements (red), and allowed Bragg reflections. $Mg_2Mn(BO_3)_2$ was 99.5% pure with a MnO_2 impurity and $Mg_2Ni(BO_3)_2$ was 99% pure with a NiO impurity.

		$Mg_2Mn(BO_3)_2$	$Mg_2Ni(BO_3)_2$
R_{wp} (%)		2.87	1.93
a (Å)		5.4836(2)	5.4008(1)
b (Å)		8.5472(4)	8.3985(1)
c (Å)		4.5500(2)	4.4813(1)
Vol ($Å^3$)		213.26(2)	203.268(5)
M1 (0, 0, 0)	Occ (Mg/*M*)	0.82/0.18(1)	0.27/0.73(1)
M2 (0, y, $\frac{1}{2}$)	Occ (Mg/*M*)	0.60/0.40(1)	0.90/0.10(1)
	y	0.3106(4)	0.3142(3)
Refined Mg/*M* ratio		2.02/0.98(3)	2.06/0.94(4)
B (x, 0, z)	x	0.255(3)	0.262(2)
	z	0.541(5)	0.549(3)
O1 (x, 0, z)	x	0.311(3)	0.323(1)
	z	0.247(3)	0.239(2)
O2 (x, y, z)	x	0.203(2)	0.2029(8)
	y	0.1422(9)	0.1399(6)
	z	0.691(1)	0.702(1)
Purity (%)		99.5(6)	99.1(4)

Table 3.2 Refined structural parameters for the orthoborates in the *Pnmn* space group. Errors are given in parentheses.

SQUID Magnetometry

A small amount of pristine $Mg_2Mn(BO_3)_2$ was set aside to measure its magnetic properties before electrochemical cycling. The results confirm that the manganese in the sample existed in the Mn^{2+} state. Using an MPMS 3 with both direct current (DC) and vibrating sample mode (VSM) for redundancy, the sample magnetic moment was measured as a function of applied magnetic field and temperature, shown in Figure 3.2. The plot in Subfigure 3.2a proves that $d\chi/dM$ is linear at 2 and 3 Tesla, so the Curie-Weiss approximation is valid. The sample moment data in Subfigure 3.2b were converted to inverse molar susceptibility and a least squares linear regression was fit between 150K and 300K shown in 3.2c and 3.2d. Using the fitted slope and equations 2.6 and 2.8, the average magnetic moment was calculated. The average of the results from the DC and VSM data at 2 T and 3 T was $5.97\mu_B$ which is in strong agreement with the known effective magnet moment for Mn^{2+} of $5.9\mu_B$.

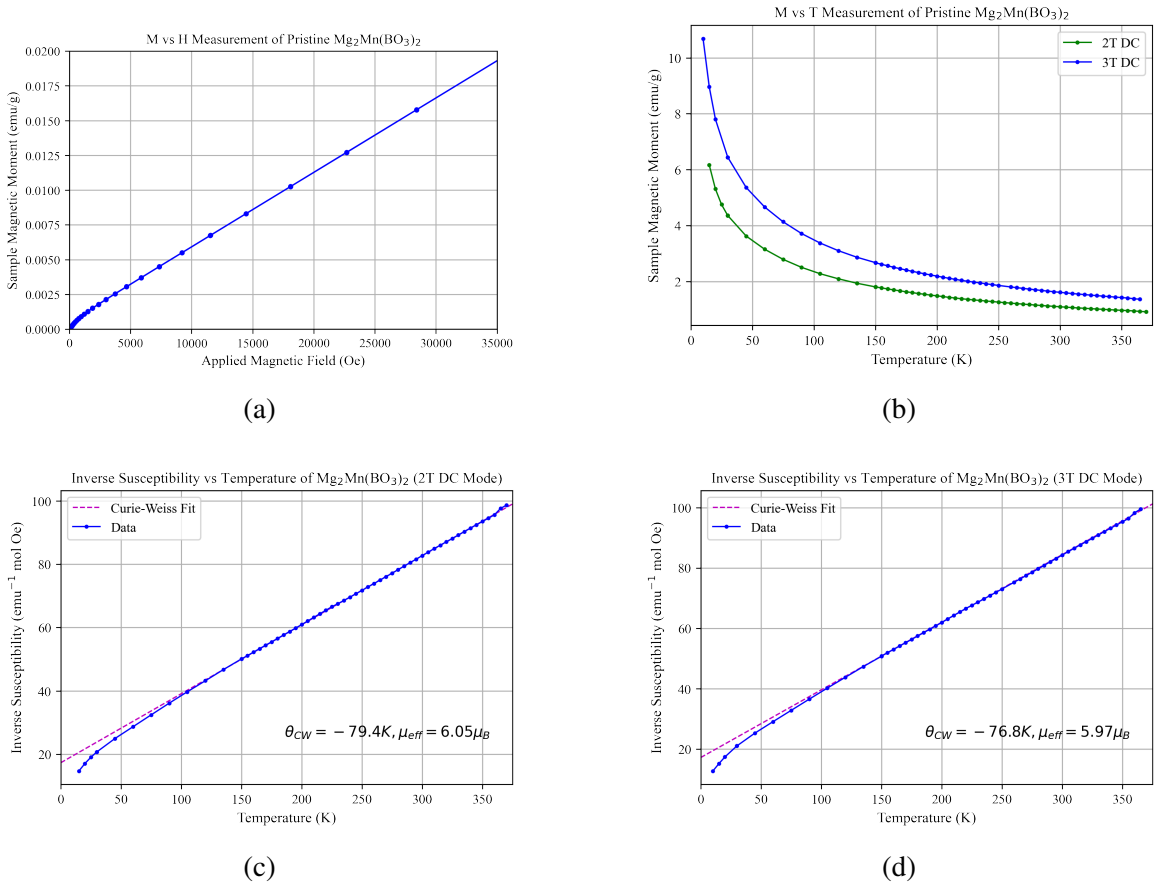

Fig. 3.2 $Mg_2Mn(BO_3)_2$ Pristine Curie-Weiss Analysis

Particle Size

In this experiment, the effects of cathode particle size reduction on electrochemical performance were investigated. Smaller cathode particles often have improved reaction kinetics because the increased surface area exposes more active sites. Additionally, there is a reduced diffusion path length for deintercalating ions, meaning they are less likely to become trapped in defects. Finally, smaller particles experience less mechanical stress during cycling, improving stability. On plots labelled "Ball-Milled," a planetary ball mill was used to grind the magnesium orthoborate before it was mixed with carbon and PVDF. Cathode sample was mixed in a 1:10 mass ratio with 3 mm zirconium dioxide balls and milled at 550 rpm for 1 hour (5 minutes on, 5 minutes off, 12 repetitions to avoid overheating). Reduction in particle size via this method was confirmed through SEM (Figure 3.3) and synchrotron XRD (Figure 3.4). Thirty-one hand-ground and ball-milled $Mg_2Mn(BO_3)_2$ particles were imaged, and the average particle size was reduced from 17(10) µm to 6(3) µm. Particle size data are detailed in Appendix B.

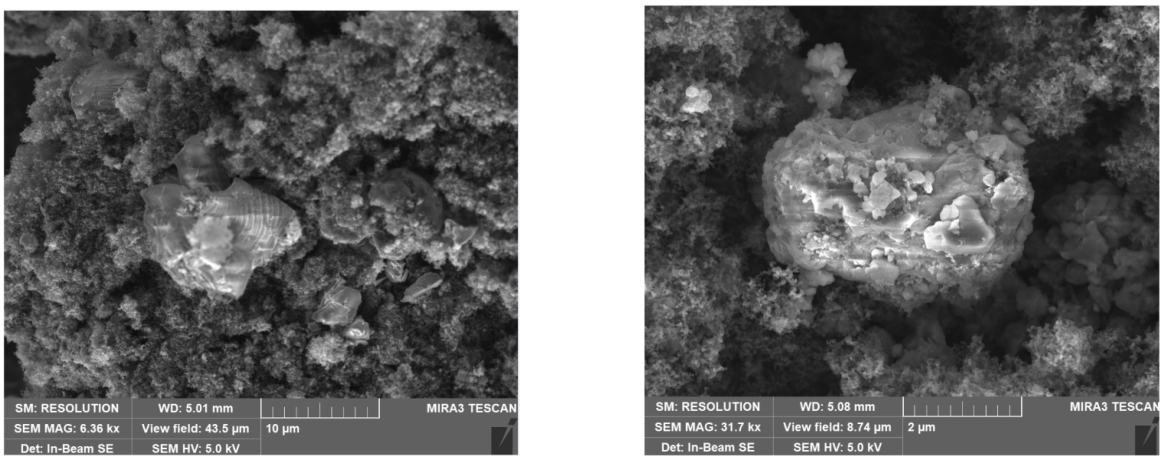

(a) (b)

Fig. 3.3 Examples of hand-ground (a) and ball-milled (b) $Mg_2Mn(BO_3)_2$ particles embedded in a carbon-PVDF matrix

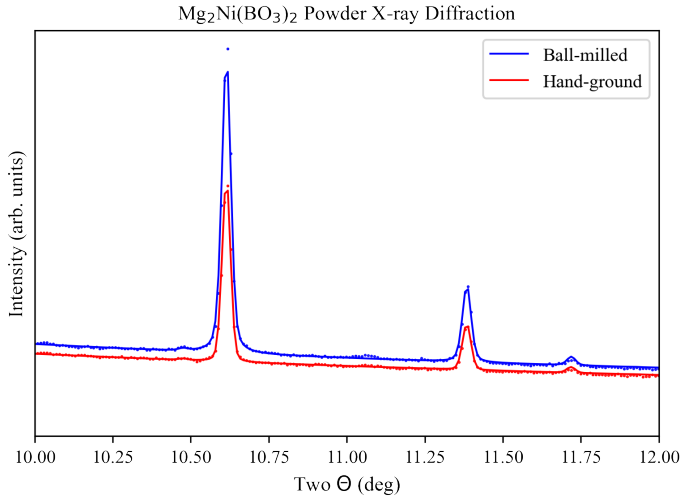

Fig. 3.4 An overlay of the hand-ground and ball-milled $Mg_2Ni(BO_3)_2$ XRD spectra showing the line broadening of smaller particles

Synchrotron XRD was performed on hand-ground and ball-milled $Mg_2Ni(BO_3)_2$ samples to measure crystallite size. SEM gives information about the overall dimensions of particles, which are composed of many crystallites and irregular in shape. XRD provides insight into the size of the ordered diffracting regions within the crystal lattice. The broadening of diffraction lines in XRD spectra can be attributed to instrument effects or physical origins. The latter consist of size-broadening and strain-broadening. In this experiment, the same diffractometer was used, so differences in peak width can be credited to physical changes induced by ball-milling. The width of a diffraction peak is inversely related to the size

of the coherent scattering regions. Smaller crystallites lead to broader peaks because the scattering from different parts of each crystallite does not perfectly reinforce each other. When performing a Rietveld refinement, peak width can be quantified in a variable called apparent domain size, D_V. D_V relates to average crystallite radius, $\overline{R}$, via the relation:

$$D_V = \frac{3}{2}\overline{R}(1+c)^3 \tag{3.1}$$

where c is a dimensionless quantity describing particle distribution [74]. Assuming a lognormal distribution of spherical crystals ($c = 0.2$), the fitted values of D_V in the $Mg_2Ni(BO_3)_2$ spectra estimate a reduction of average radius from 13.3(1.8) nm to 4.8(5) nm after ball milling, confirming a reduction in size.

3.1.3 Electrochemistry

$Mg_2Mn(BO_3)_2$

In $Mg_2Mn(BO_3)_2$, removal of one Mg ion per formula unit on charge to get $MgMn^{4+}(BO_3)_2$ would yield a theoretical capacity of 242.3 $mAhg^{-1}$. The subsequent insertion of two Li^+ on discharge would yield a theoretical capacity of 272.3 $mAhg^{-1}$. As seen in Figure 3.5, when cycled at room temperature, specific capacities around 27 $mAhg^{-1}$ and 31 $mAhg^{-1}$ were achieved on charge and discharge, respectively.

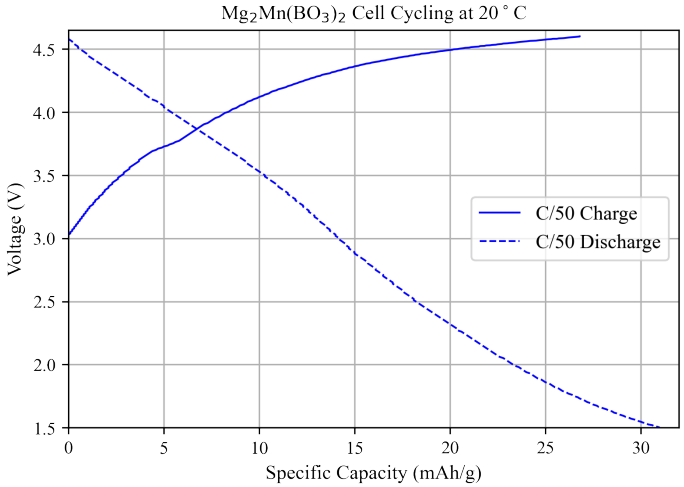

Fig. 3.5 $Mg_2Mn(BO_3)_2$ cycling behaviour vs. a Li metal anode at 20°C at a rate of C/50 between 1.5 V and 4.6 V

To improve diffusion kinetics, cells were cycled at 55°C. Shown in Figure 3.6, these cells achieved specific capacities up to 175 $mAhg^{-1}$ on charge and 65 $mAhg^{-1}$ on discharge.

The charge profile exhibited two voltage plateaus at 3.5 V and 4.5 V. Cells cycling under identical conditions, but prepared using ball-milled cathode crystals exhibited the same voltage plateaus at 3.5 V and 4.5 V, and achieved specific capacities up to 195 $mAhg^{-1}$ on charge and 62 $mAhg^{-1}$ on discharge as seen in Figure 3.14. One notable consequence of ball milling was the lengthening of the chemical process causing the 3.5 V plateau. In the hand ground samples, it occurred over a range less than 30 $mAhg^{-1}$. In the ball milled samples, this range increased to 60 $mAhg^{-1}$, shown in Figure 3.7. The behavior on first charge is significantly different than that on subsequent charges because it involved magnesium, while the latter are attributed to lithium intercalation.

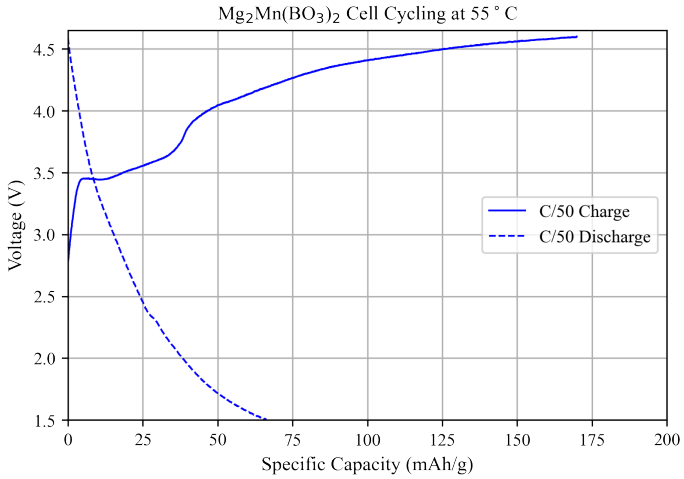

Fig. 3.6 $Mg_2Mn(BO_3)_2$ cycling behaviour vs. a Li metal anode at 55°C at a rate of C/50 between 1.5 V and 4.6 V

$Mg_2Ni(BO_3)_2$

In $Mg_2Ni(BO_3)_2$, removal of one Mg ion per formula unit on charge to get $MgNi^{4+}(BO_3)_2$ would yield a theoretical capacity of 238.3 $mAhg^{-1}$. The subsequent insertion of two Li^+ on discharge would yield a theoretical capacity of 267.2 $mAhg^{-1}$. As seen in Figure 3.8, when cycled at room temperature, a specific capacity of 28 $mAhg^{-1}$ was achieved on charge and discharge. The sloping, featureless profile and the low capacities again indicated poor redox reactions. After ball milling, there was no increase in the overall specific capacity reached at room temperature; however, the 3.5 V plateau appeared during charging, shown in Figure 3.9. To investigate how much capacity could be achieved through increased ball milling, the cathode powder was ball milled for 6 hours instead of 1, following the same procedure outlined in Section 3.1.2. Cells with this material achieved specific capacities up

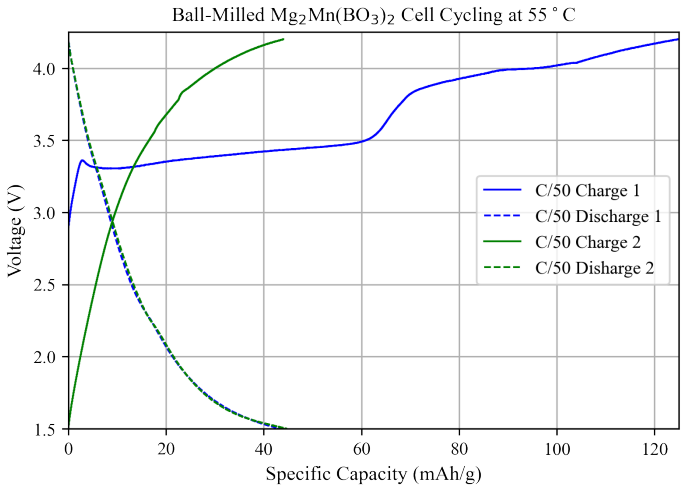

Fig. 3.7 Ball-milled $Mg_2Mn(BO_3)_2$ cycling behaviour vs. a Li metal anode at 20°C at a rate of C/50 between 1.5 V and 4.2 V

to 85 $mAhg^{-1}$ on charge and 52 $mAhg^{-1}$ on discharge with a longer feature at 3.5 V, shown in Figure 3.10.

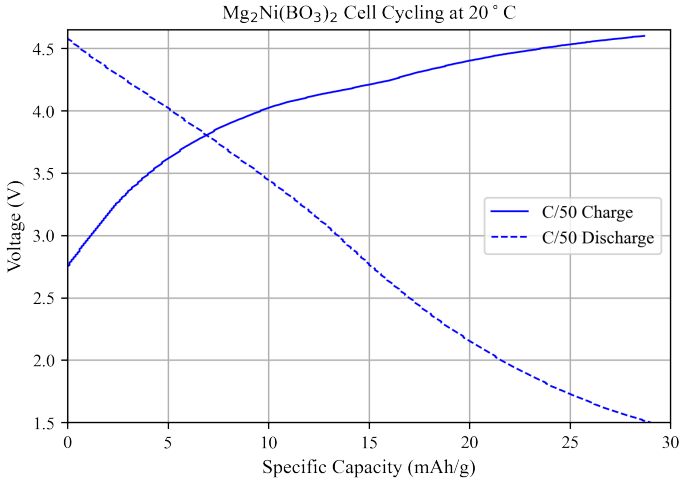

Fig. 3.8 $Mg_2Ni(BO_3)_2$ cycling behaviour vs. a Li metal anode at 20°C at a rate of C/50 between 1.5 V and 4.6 V

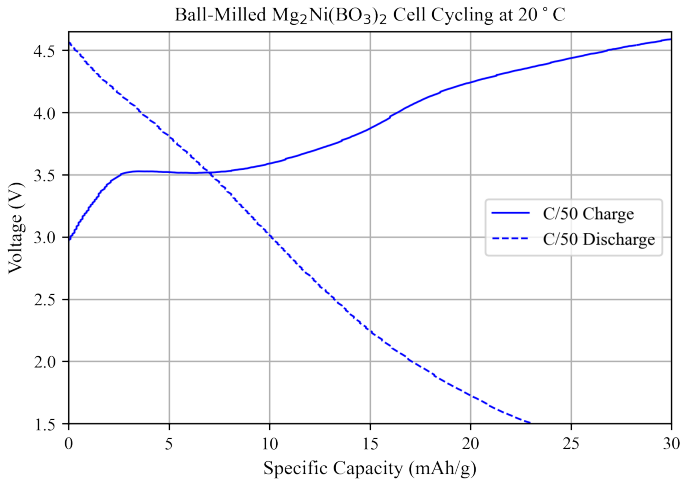

Fig. 3.9 Ball-milled $Mg_2Ni(BO_3)_2$ cycling behaviour vs. a Li metal anode at 20°C at a rate of C/50 between 1.5 V and 4.6 V

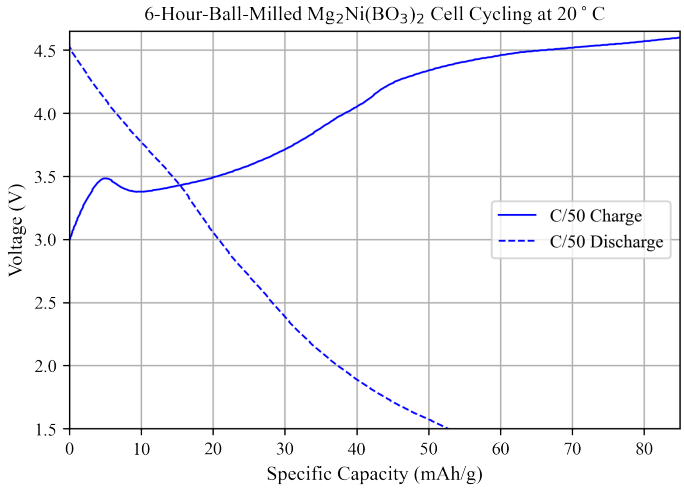

Fig. 3.10 6-hour ball-milled $Mg_2Ni(BO_3)_2$ cycling behaviour vs. a Li metal anode at 20°C at a rate of C/50 between 1.5 V and 4.6 V

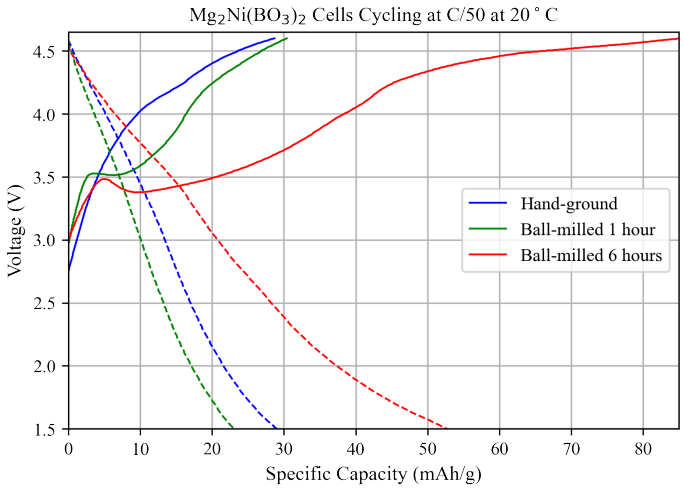

Fig. 3.11 $Mg_2Ni(BO_3)_2$ cycling behaviour vs. a Li metal anode at 20°C at a rate of C/50 between 1.5 V and 4.6 V, exemplifying the effects of ball milling

To improve diffusion kinetics, cells were cycled at 55°C. Shown in Figure 3.12, these cells achieved specific capacities up to 92 $mAhg^{-1}$ on charge and 43 $mAhg^{-1}$ on discharge. The charge profile exhibited two voltage plateaus at 3.5 V and 4.5 V. Cells cycling under identical conditions, but made using ball-milled cathode crystals exhibited the same voltage plateaus at 3.5 V and 4.5 V, and achieved higher specific capacities as seen in Figure 3.13. As with the manganese-containing orthoborate, one notable consequence of ball milling was the lengthening of the chemical process causing the 3.5 V plateau. In the hand ground samples, it occurred over a range less than 30 $mAhg^{-1}$. In the ball milled samples, this range increased to 80 $mAhg^{-1}$. Again, the behavior on first charge is significantly different than that on subsequent charges.

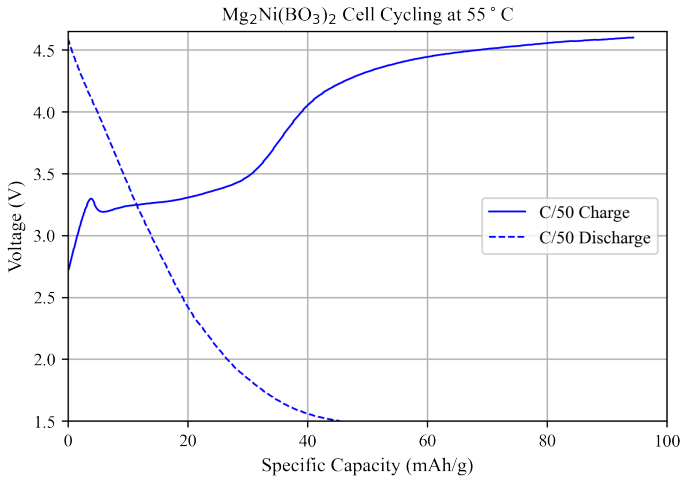

Fig. 3.12 $Mg_2Ni(BO_3)_2$ cycling behaviour vs. a Li metal anode at 55°C at a rate of C/50 between 1.5 V and 4.6 V

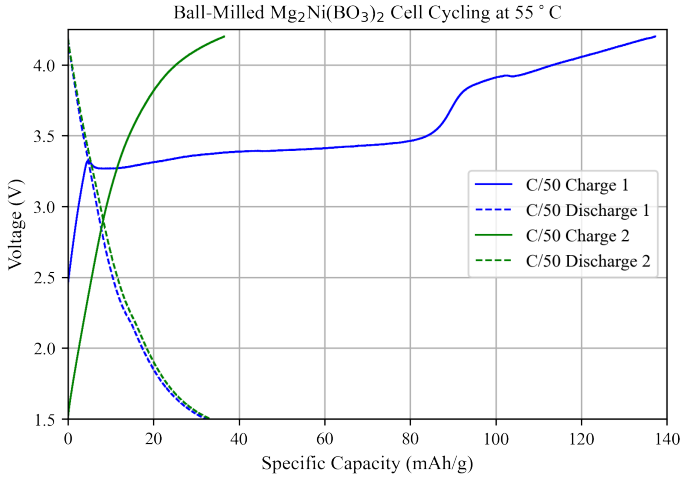

Fig. 3.13 Ball-milled $Mg_2Ni(BO_3)_2$ cycling behaviour vs. a Li metal anode at 55°C at a rate of C/50 between 1.5 V and 4.2 V

3.1.4 Post-Cycling Analysis

The high capacities achieved by both the $Mg_2Mn(BO_3)_2$ and $Mg_2Ni(BO_3)_2$ cathodes on first charge as well as the long voltage plateaus are promising signs of viability. In order to prove that a reversible magnesium intercalation reaction is taking place, the cathodes must be cycled many times vs. a magnesium anode or subjected to rigorous analysis after the first charge. Because an effective magnesium-based electrolyte does not exist, the first option is

not currently possible. The second was therefore pursued. $Mg_2Mn(BO_3)_2$ cathode samples were collected at four sites along the charge profile at 55°C for a 1 hour ball-milled sample: pristine, charged to 3.6 V (after the first plateau), charged to 4.6 V (after the second plateau), and charged to 4.6 V then discharged to 1.5 V as indicated in Figure 3.14.

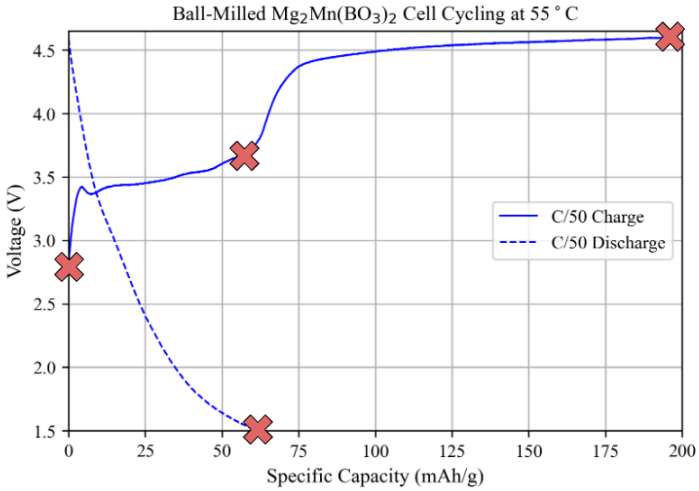

Fig. 3.14 Ball-milled $Mg_2Mn(BO_3)_2$ cycling behaviour vs. a Li metal anode at 20°C at a rate of C/50 between 1.5 V and 4.6 V. The red crosses indicate where cycling was stopped and samples were collected.

XRD

If demagnesiation is occurring during charge and lithiation is occurring during discharge, then there will be measurable effects on the synchrotron XRD profiles of cathode crystals at each of the four sites probed, shown in Figure 3.15. These will manifest as changes in the relative amplitudes of peaks in the spectra or changes in the peak positions indicating volume change. Magnesium removal ought to result in change of the unit cell volume and changes in the fitted site occupancies. In a previous study on a $LiMg_{0.01}Co_{0.99}O_2$ cathode, XRD revealed that the unit cell volume changed from 96.3 $Å^3$ to 98.3 $Å^3$ upon 60% Li removal [75]. In the polyanion cathode, $LiFePO_4$, XRD revealed that upon 85% delithiation, the unit cell volume decreased from 292 $Å^3$ to 287 $Å^3$ [76]. Changes of this magnitude are within the resolution of a Rietveld refinement performed on synchrotron XRD data, so should a similar volume change occur in magnesium orthoborates, it would be detected. Rietveld refinements on spectra gathered from each of the four states of charge showed no change in the unit cell volume within the error margins: 213.26(2) $Å^3$. Additionally, when the manganese occupation was constrained to the pristine fitted value, the fitted magnesium occupation values did not change outside of the error margins for the charge sites probed.

These data are presented in Appendix C. This evidence suggests that magnesium was not deintercalating from the cathode during charge, and another electrochemical process was responsible for the observed charge profiles. One notable feature was the appearance of a small peak at $2\theta = 11.5^{\circ}$ in the 4.6 V charge XRD spectrum. This peak was not an allowed Bragg reflection and corresponded to an unidentified phase.

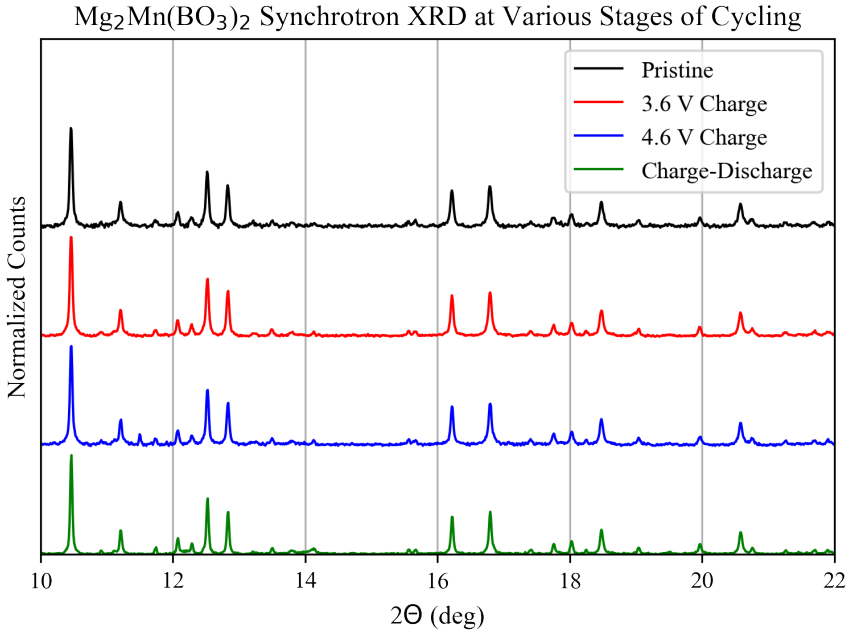

Fig. 3.15 $Mg_2Mn(BO_3)_2$ ex situ normalized XRD spectra collected with $\lambda = 0.4938100$ Å

SEM-EDX

EDX maps, like that shown in Figure 3.16, collected from 14 pristine $Mg_2Mn(BO_3)_2$ particles and 4 particles charged to 4.6 V showed that the average Mg:Mn ratio went from 2.08(16):1 to 2.23(11):1 after charging. These data are presented in Appendix D. They do not support the conclusion that magnesium is being deintercalated from the cathode, as there was no statistically significant change.

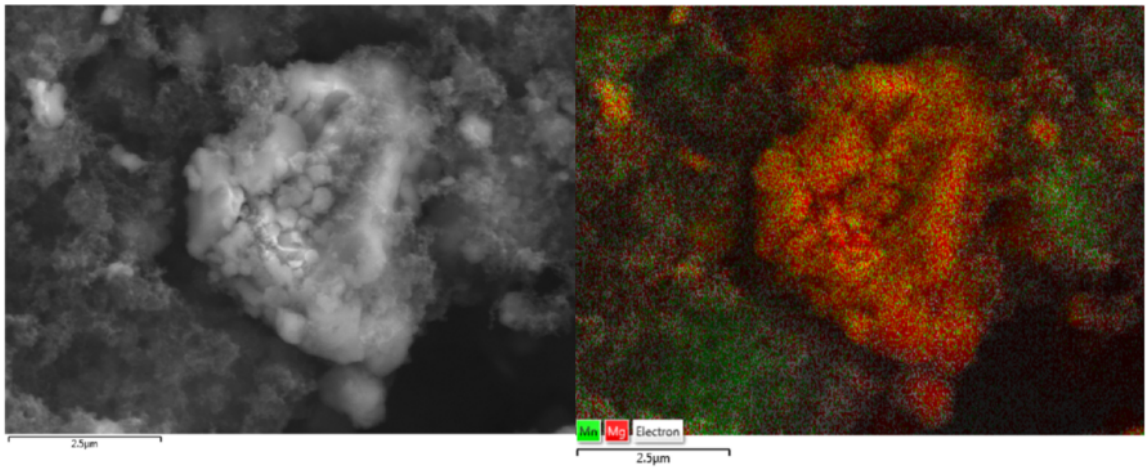

Fig. 3.16 Left: an SEM image of an $Mg_2Mn(BO_3)_2$ particle. Right: an example EDX map of that particle showing manganese in green and magnesium in red.

XANES Spectroscopy

XRD and SEM-EDX were used to directly investigate magnesium deintercalation. XANES spectroscopy was used to indirectly investigate magnesium deintercalation by probing transition metal oxidation. If demagnesiation occurs, manganese in the cathode will undergo oxidation to balance charge in the system. This will result in detectable changes in the XANES spectra shown in Figure 3.17. $Mg_2Mn(BO_3)_2$ operando cells were cycled at room temperature at charge rates ranging from C/50 to C/100 to maximize capacity, while XANES spectra were collected near the manganese K-edge using the B18 spectrometer at Diamond Light Source. In every cell across the entire charge profile, there were no changes in the spectra, supporting the conclusion that manganese oxidation was not taking place.

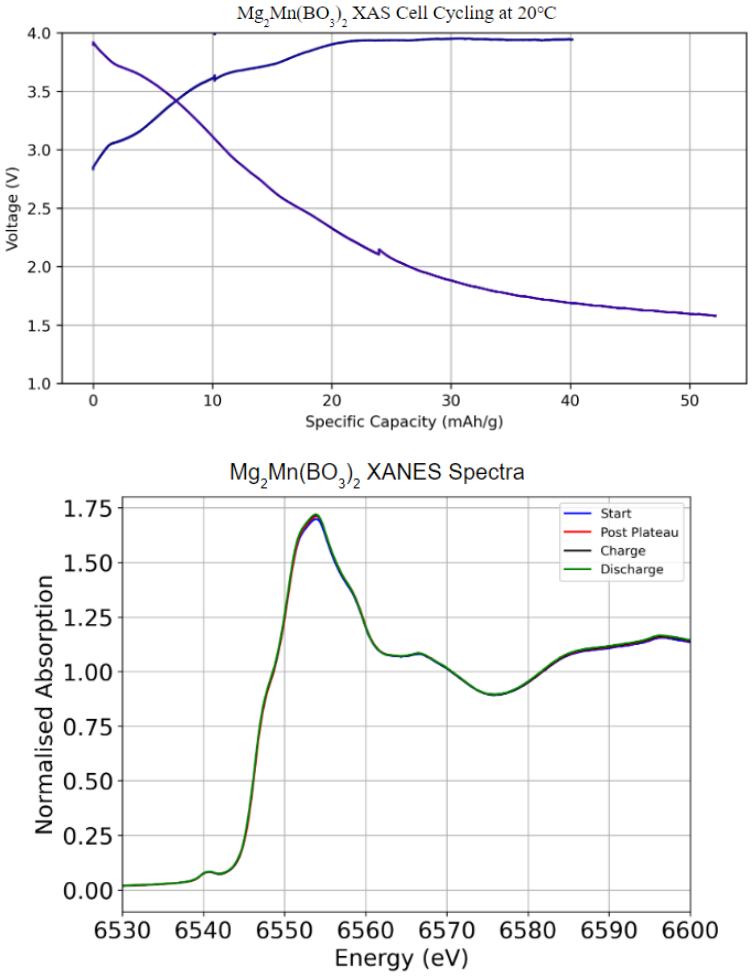

Fig. 3.17 Electrochemistry and XANES spectra of an $Mg_2Mn(BO_3)_2$ cell cycled at C/50 at 20°C. The four spectra were collected before cycling, charged to 3.75 V, charged to 3.99 V, and after discharge.

"*Power* ought to serve as a check to *power*." - Baron de Montesquieu

3.2 $LiFeBO_3$

Thus far, $Mg_2Mn(BO_3)_2$ and $Mg_2Ni(BO_3)_2$ cells exhibited promising electrochemistry on first charge, having high specific capacities and long voltage plateaus. Despite this promise, XRD, SEM-EDX, and XANES analyses on $Mg_2Mn(BO_3)_2$ cells did not support the conclusion that magnesium deintercalation was the responsible mechanism. It was postulated that the high temperatures and low charge rates could have caused corrosion of the steel coin cell which contributed to the observed capacities. In order to rule out that the electrochemistry was a consequence of the experimental setup, $LiFeBO_3$ cells were constructed and cycled under identical conditions. $LiFeBO_3$ is a widely-studied polyanion cathode in lithium-ion batteries. If published electrochemistry could be reproduced, it would support the conclusion that the observed magnesium orthoborate electrochemistry was a property of the material, not the apparatus and experimental protocol.

3.2.1 Synthesis

There are many different published synthesis routes for $LiFeBO_3$ [77, 78]. After 9 synthesis attempts (detailed in Appendix E) achieving varying degrees of purity, phase pure $LiFeBO_3$ was synthesized via the following procedure. Using a mortar and pestle, stoichiometric amounts of lithium hydroxide monohydrate ($LiOH{\cdot}H_2O$), iron (II) oxalate dihydrate ($FeC_2O_4{\cdot}2H_2O$), and boric acid (H_3BO_3) were ground for 10 minutes. This powder was placed in an alumina crucible wrapped in copper foil and heated in a tube furnace with flowing Ar to 350°C for 10 hours using a heating rate of 3°C/min. After cooling naturally, the powder was reground, pressed into a 13 mm pellet, and reheated to 650°C for 10 hours using a heating rate of 3°C/min.

3.2.2 Material Characterization

Powder XRD confirmed synthesis of the intended phase. Synthesis 8 had a 1.91(05)% Fe metal impurity, shown in the synchrotron XRD spectrum in Figure 3.18. An XRD spectrum collected on synthesis 9 using the Bruker D8 revealed no impurities.

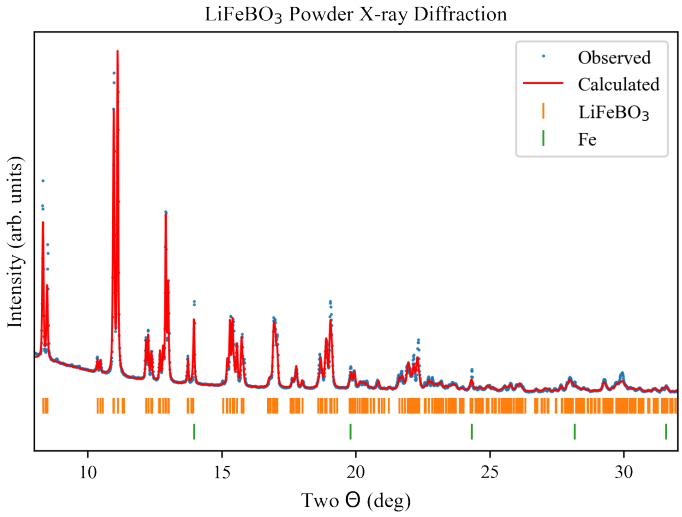

Fig. 3.18 $LiFeBO_3$ synchrotron XRD (blue) collected with with $\lambda = 0.493168$ Å, Rietveld refinements (red), and allowed Bragg reflections. $R_{wp} = 8.54\%$

3.2.3 Cycling Performance

$LiFeBO_3$ has a theoretical capacity of 220.41 $mAhg^{-1}$. $LiFeBO_3$ cells were made with Super P and Ketjenblack carbon and cycled up to 10 times at C/20 and C/50 at 20°C. Shown in Figures 3.19 and 3.20, the cells achieved reversible capacities around 40 $mAhg^{-1}$ when made with Super P and 120 $mAhg^{-1}$ when made with Ketjenblack. The charge curves exhibited two shoulders at 2.1 V and 2.85 V. The discharge curves exhibited a shoulder at 1.5 V. The first charges behaved significantly differently than subsequent charges, having a 3.0 V plateau and much lower capacities. This is attributed to the oxidation of iron in a small $LiFeO_2$ impurity during the first charge [79]. Importantly, the overall cycling behavior was different from the magnesium orthoborates and matched published results [80, 79]. This suggested that the electrochemistry of the magnesium orthoborates at 20°C was a material property, not a consequence of experimental design.

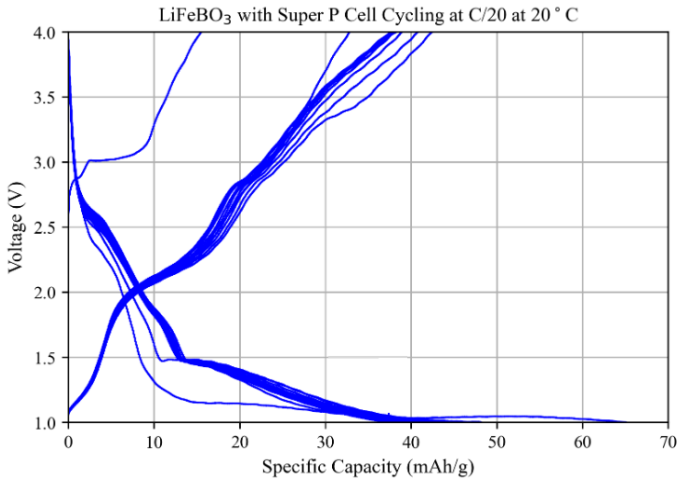

Fig. 3.19 $LiFeBO_3$ with Super P cycling behaviour vs. a Li metal anode at 20°C at a rate of C/20 between 1.0 V and 4.0 V (7 cycles)

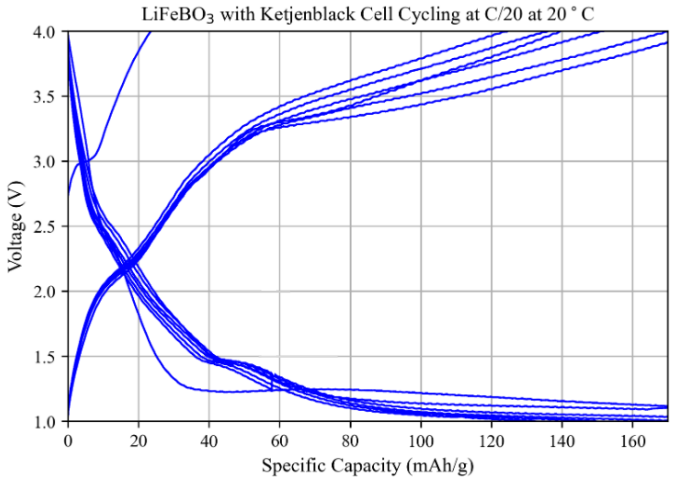

Fig. 3.20 $LiFeBO_3$ with Ketjenblack cycling behaviour vs. a Li metal anode at 20°C at a rate of C/20 between 1.0 V and 4.0 V (7 cycles)

$LiFeBO_3$ cells were made with Super P and Ketjenblack carbon and cycled up to 5 times at C/50 at 55°C. Shown in Figures 3.21 and 3.22, the cells achieved reversible capacities around 45 $mAhg^{-1}$ when made with Super P and 100 $mAhg^{-1}$ when made with Ketjenblack. The discharge curves exhibited a clear plateau at 2.7 V attributed to Fe^{3+}/Fe^{2+} reduction [81]. Again, the overall cycling behavior was different from the magnesium orthoborates and matched published results [78, 81]. This proved that real capacities, owed to intercalation, could be reproduced when cycling a borate cathode using the construction techniques, low cycling rate (C/50), and high temperature (55°C) of this experiment. This suggested that

the electrochemistry of the magnesium orthoborates at 55°C was a material property, not a consequence of experimental design. It is possible, however, that when a magnesium orthoborate cathode is used, the activation energy required for it to undergo oxidation is above the energy required for degradation of the steel casing. This means that the capacities observed when cycling the orthoborates could in fact be attributed to steel degradation which has been documented in other studies with non-aqueous electrolytes at high voltages [82]. In summary, the $LiFeBO_3$ electrochemistry proves the efficacy of the experimental design to test cathodes, but further examination of the steel casing before and after cycling would be necessary to completely rule out steel degradation.

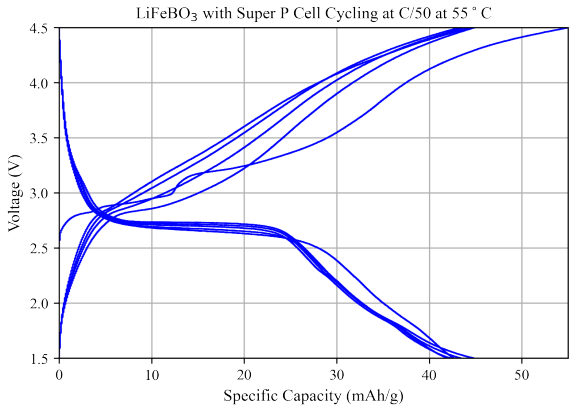

Fig. 3.21 $LiFeBO_3$ with Super P cycling behaviour vs. a Li metal anode at 55°C at a rate of C/50 between 1.5 V and 4.5 V (5 cycles)

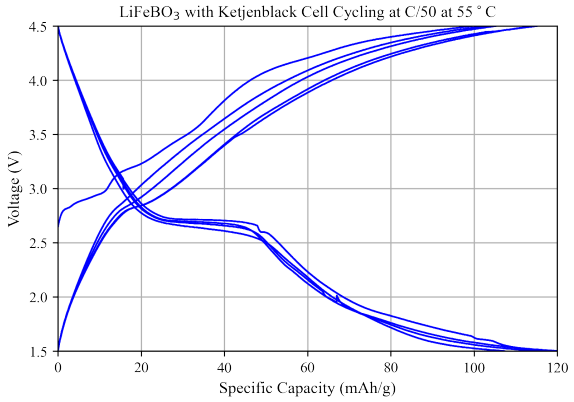

Fig. 3.22 $LiFeBO_3$ with Ketjenblack cycling behaviour vs. a Li metal anode at 55°C at a rate of C/50 between 1.5 V and 4.5 V (5 cycles)

"*Power* is given only to those who dare to lower themselves and pick it up. Only one thing matters, one thing; to be able to dare!" - Fyodor Dostoevsky

3.3 $Mg_3(BO_3)_2$

Both $Mg_2Mn(BO_3)_2$ and $Mg_2Ni(BO_3)_2$ achieved high specific capacities on first charge, yet testing on $Mg_2Mn(BO_3)_2$ showed that demagnesiation was not the mechanism responsible. The $LiFeBO_3$ control experiments confirmed that delithiation was possible under identical conditions. The remaining experiments were undertaken to uncover the redox reaction causing the observed capacities.

The two magnesium-transition metal orthoborates exhibited an identical voltage plateau at 3.5 V which was lengthened by ball milling. This led to suspicion that transition metal oxidation was not the responsible mechanism because Mn and Ni ought to have different oxidation energies in the material. To confirm that Mn and Ni were not involved in the reaction, cells were constructed with $Mg_3(BO_3)_2$. $Mg_3(BO_3)_2$ is not known to be electrochemically active.

3.3.1 Synthesis and Characterization

$Mg_3(BO_3)_2$ was synthesized by mixing MgO and H_3BO_3 in a stoichiometric ratio and following the same grinding, pelletizing, and heating procedure as $Mg_2Ni(BO_3)_2$. Powder XRD, shown in Figure 3.23, was collected on the Bruker D8. It revealed the $Mg_3(BO_3)_2$ to be 95.5(2)% pure with a 4.5(2) wt.% $Mg_2B_2O_5$ impurity.

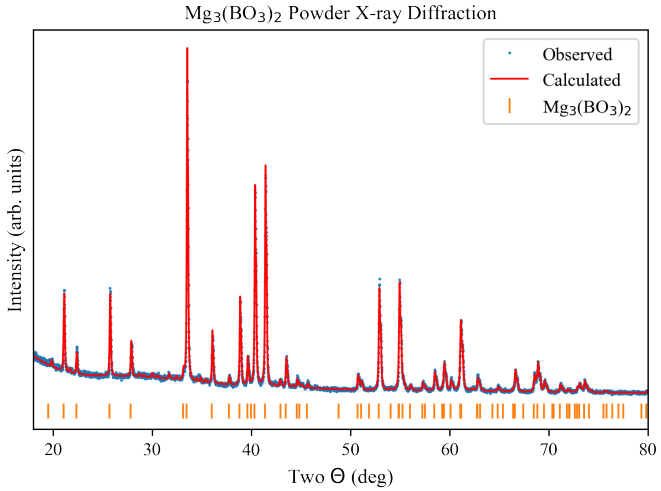

Fig. 3.23 $Mg_3(BO_3)_2$ XRD (blue) collected with λ = 1.54060 Å, Rietveld refinements (red), and allowed Bragg reflections. R_{wp} = 5.86%.

3.3.2 Cycling Performance

Seen in Figure 3.24, specific capacities of 81 $mAhg^{-1}$ and 51 $mAhg^{-1}$ were achieved on charge and discharge, respectively at 55°C. The 3.5 V plateau was present in this material, proving that the electrochemical process is not dependent upon the transition metals. Figure 3.25 shows how similar this charge profile is the other hand-ground orthoborates.

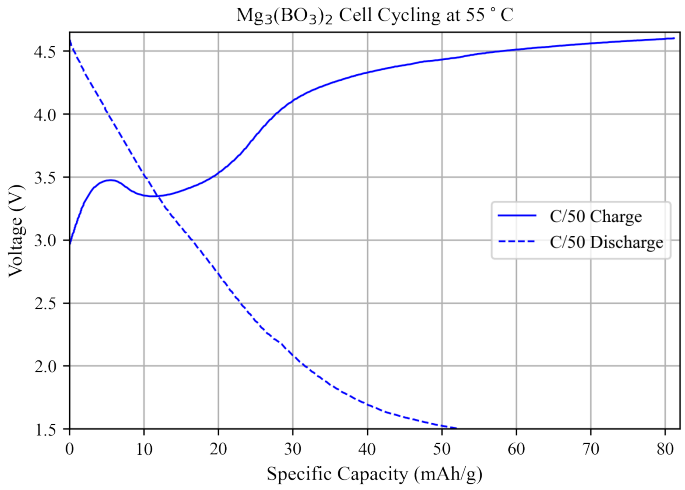

Fig. 3.24 $Mg_3(BO_3)_2$ cycling behaviour vs. a Li metal anode at 55°C at a rate of C/50 between 1.5 V and 4.6 V

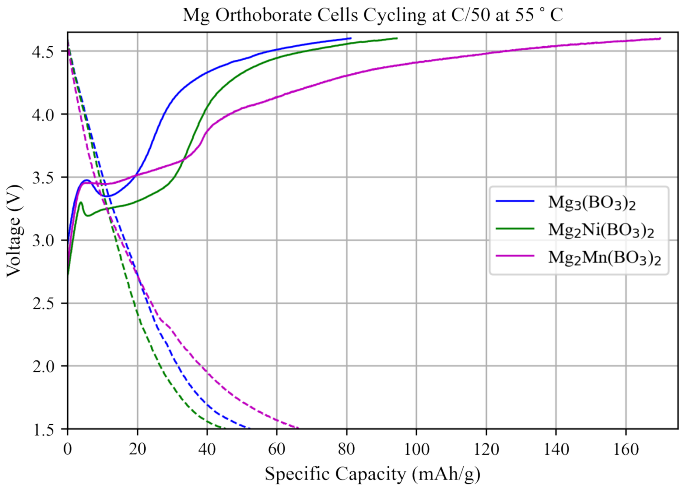

Fig. 3.25 $M_3(BO_3)_2$ cycling behaviour vs. a Li metal anode at 55°C at a rate of C/50 between 1.5 V and 4.6 V

"*Power* concedes nothing without a demand. It never did and it never will." - Frederick Douglass

3.4 Amorphous Borate Redox

Under the tested conditions, magnesium orthoborates did not show promise as rechargeable cathode materials. At room temperature, less than 15% of the theoretical capacity was achieved. At high temperature, despite the large capacities on first charge, testing revealed magnesium deintercalation was not occurring. The final step necessary to complete the narrative on these materials was to ascertain the redox reaction which was happening. In the $LiFeBO_3$ experiments, Ketjenblack caused increased, but still real, capacities. In the $Mg_3(BO_3)_2$ experiments, transition metals were eliminated as contributing factors.

In electrochemical tests on Li_2MnO_3, it was shown that ball milling the cathode resulted in increased capacities as well as CO_2 and O_2 gas production during cycling [83]. This was attributed to the introduction of Li_2CO_3 during ball-milling. In order to investigate if confounding carbonate species were present in the magnesium orthoborates, IR spectroscopy was performed both before and after ball milling.

3.4.1 IR Spectroscopy

IR spectra were collected on $Mg_2Mn(BO_3)_2$ and $Mg_2Ni(BO_3)_2$ before and after ball milling, as well as magnesium carbonate ($MgCO_3$). The characteristic peaks associated with $MgCO_3$ were not present in the orthoborate spectra. This suggested that carbonate species were not present in the samples either before or after ball milling, although it did not entirely rule out the possibility because the amplitude of these peaks may have been obfuscated by significantly larger orthoborate peaks.

When comparing two IR spectra from the same material prepared under different conditions, the appearance of new peaks or the change in relative magnitudes of existing peaks are features to note. One appreciable difference between the IR spectra of the hand-ground and ball-milled samples was the appearance of new features after ball milling. Shown in Figure 3.26, around 1450 cm^{-1} a raised shoulder is present in the ball-milled samples which is absent in the hand-ground sample. Also, the peak at 1050 cm^{-1} is clear in the ball-milled samples and barely visible in the hand-ground sample. It has been shown that lithium borate glasses ($xLi_2O{\cdot}(1\text{-}x)B_2O_3$) exhibit peaks at these locations [69]. Lithium borate glasses have been shown to function as high-capacity cathode materials in recent studies [84–86]. One theory is that amorphous borate impurities acted as the sites for redox reactions in these

materials. The increased energy and strain introduced by ball-milling created more of these amorphous species, leading to the higher capacities and the lengthening of the 3.5 V plateau.

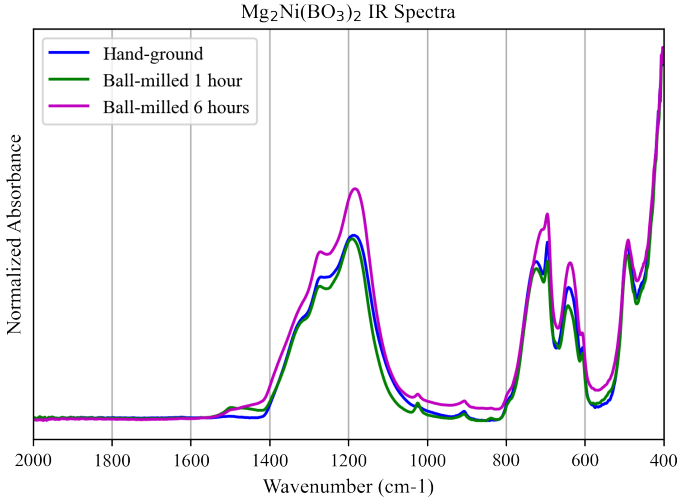

Fig. 3.26 Normalized $Mg_2Ni(BO_3)_2$ IR spectra collected on hand-ground, 1-hour ball-milled, and 6-hour ball-milled samples

Chapter 4

Conclusion

"*Power* gradually extirpates from the mind every humane and gentle virtue." - Edmund Burke

Summary

Rechargeable batteries are an integral part of modern civilization. There is a present and growing demand for them in portable electronics, electric vehicles, and grid energy storage. Cost, safety, and performance concerns in lithium-ion batteries, which account for the largest market share among battery chemistries, have invited research into alternate materials. One such candidate is magnesium. Magnesium is 1200 times more abundant than lithium and 20 times cheaper. The lack of dendrite growth and superior volumetric capacity mean improved safety and performance than lithium-ion batteries. The scientific hurdles impeding the production of a rechargeable magnesium-ion intercalation battery are the cathode and the electrolyte.

In this project, I sought to study the efficacy of magnesium orthoborates, $Mg_2M(BO_3)_2$ M = Mn, Ni, as magnesium intercalation cathodes. When cycled at room temperature vs. a lithium metal anode, capacities up to 30 $mAhg^{-1}$ are extracted on first charge. At 55°C, this is increased up to 200 $mAhg^{-1}$. Both materials undergo an electrochemical process causing a voltage plateau at 3.5 V. This plateau is lengthened by ball milling the cathode. Synchrotron XRD spectra collected on $Mg_2Mn(BO_3)_2$ cathode samples across the charge curve did not show changes in unit cell volume or crystal site occupations. SEM-EDX maps collected on pristine and charged $Mg_2Mn(BO_3)_2$ particles did not show a reduction in the atomic ratio of magnesium relative to manganese. Finally, XANES spectra collected on $Mg_2Mn(BO_3)_2$ cells at room temperature throughout the charge process did not support the conclusion of transition metal oxidation. Together, these results showed that despite achieving high

capacities on first charge, these materials do not act as magnesium intercalation compounds, as was previously reported [62].

$LiFeBO_3$ was synthesized and tested as a cathode material using an experimental setup identical to that used for $Mg_2M(BO_3)_2$. Published electrochemistry was reproduced and the reversible (de)intercalation of Li occurred over multiple cycles. Evidently, the behaviors and capacities of the magnesium orthoborates could be credited to the materials and likely not degradation of the cell or some other apparatus abnormality.

To investigate the role of the transition metal in the electrochemical process of the magnesium orthoborates, cells were constructed using an $Mg_3(BO_3)_2$ cathode. These cells achieved capacities up to 80 $mAhg^{-1}$ and displayed the same general charge profile as the $Mg_2M(BO_3)_2$ orthoborate cathodes. This demonstrated that the mechanism responsible for the observed capacities was a property of magnesium borates prepared via this method.

Finally, in a first attempt to possibly elucidate the redox mechanism responsible for the observed capacities, IR spectroscopy was performed on the cathode powders before and after ball milling for 1 or 6 hours. The IR spectra showed no signs of carbonate impurities, but did exhibit changes before and after ball milling. The appearance of a shoulder at 1450 cm^{-1} and the increase in the relative intensity of the 1050 cm^{-1} absorbance peak suggested the possibility that an amorphous borate compound was present in the materials and its presence was increased after the energy and strain introduced by ball milling the cathode.

Further Work

The magnesium orthoborates did not function as intercalation compounds under the tested conditions, but it is feasible that they may work under different conditions. Although unlikely, different synthesis procedures, alternate electrolyte selections, or surface coatings could positively affect the electrochemistry. In order to determine an appropriate course of action, it is necessary to correctly identify the mechanism which is causing the high capacities on first charge. The lack of evidence supporting deintercalation as well as the electrochemistry's dependence on ball milling indicate that it is likely a conversion reaction taking place between electrolyte species and the cathode crystals or impurities in the cathode. To correctly identify the reactants, differential electrochemical mass spectrometry (DEMS) could be performed to identify the formation of gaseous byproducts. The next logical step in this experiment is to construct electrochemical cells out of the magnesium orthoborate materials after only the first heat. If amorphous borate compounds are contributing to the observed capacities, they will be present after the first heating. Next, perform X-ray pair distribution function (XPDF) analysis on the cathode powders. XPDF is different from X-ray crystallography because by performing a Fourier transform on X-ray diffraction data, it provides information

on the distribution of distances between pairs of atoms within a material. This can identify the presence of borate glasses containing B_2O_3 units which may have caused confounding capacity contributions. By isolating and electrochemically testing any amorphous borate compounds in these materials, one can correctly attribute the capacity contributions. This will enable informed decisions to be made on the efficacy of these materials and future magnesium-ion battery research.

References

[1] António Guterres. Secretary-General's speech on the launch of the World Meteorological Organization's State of the Global Climate 2021 Report. 18 May 2022.

[2] Brandon Miller. These US cities had the coldest monring in decades–with some reaching all-time record lows. *CNN*, 16 February 2021.

[3] Jess Donald. Winter Storm Uri 2021 The Economic Impact of the Storm. *Texas Comptroller of Public Accounts*, October 2021.

[4] Patrick Svitek. Texas puts final estimate of winter storm death toll at 246. *The Texas Tribune*, 22 January 2022.

[5] Jeff Masters. Death Valley, California, may have recorded the hottest temperature in world history. *Yale Climate Connections*, 17 August 2020.

[6] California Energy Commission. Final Root Cause Analysis Mid-August 2020 Extreme Heat Wave. 13 January 2021.

[7] Eaton Corporation. Blackout Tracker United States Annual Report. 2018.

[8] Teddy Gonzalez and Jillian Knox. In the dark: The scapegoating of renewables after grid failures. *Natural Resources Journal*, 63(1):30–69, 2023.

[9] Oliver Smith, Oliver Cattell, Etienne Farcot, Reuben D. O'Dea, and Keith I. Hopcraft. The effect of renewable energy incorporation on power grid stability and resilience. *Science Advances*, 8(9), 2022.

[10] Gavin Newsom. Wallis Annenberg Wildlife Crossing speech. 22 April 2022.

[11] Sylvester Turner. Earth Day speech. 22 April 2021.

[12] SB-1020 Clean Energy, Jobs, and Affordability Act of 2022. 16 September 2022.

[13] California Energy Commission. 2021 Total System Electric Generation. 2022.

[14] Texas' Energy Profile A Review of the State's Current Traditional and Renewable Energy Capabilities. *Texas Comptroller of Public Accounts*, September 2022.

[15] Hana Colwell. Clean Energy in America Reaches Milestone in 2021, But Installation Pace Must Accelerate to Reach Emissions Goals. *CleanPower.org*, 16 February 2022.

[16] Elon Musk. 60 Minutes. *CBS*, 28 October 2017.

[17] Hannah Ritchie. What are the safest and cleanest sources of energy? *Our World in Data*, 10 February 2020.

[18] James Conca. Natural Gas Industry Blasts Nuclear Power With Fake News. *Forbes*, 15 July 2017.

[19] United Nations. Fact Sheet Climate Change. 16 October 2021.

[20] Richard Disney. How have the forecasts on the effect of sanctions on Russia held up a year on? *Economics Observatory*, 26 April 2023.

[21] Oak Ridge National Laboratory. All-Electric Vehicles. *fueleconomy.gov*, 2023.

[22] Oak Ridge National Laboratory. Where the Energy Goes: Electric Cars. *fueleconomy.gov*, 2023.

[23] Christian Seabaugh and Renz Dimaandal. 2022 Tesla Model S Plaid First Test: 0–60 MPH in 1.98 Seconds. *MOTORTREND*, 17 June 2021.

[24] US Department of Energy Vehicle Technologies Office. Model Year 2021 All-Electric Vehicles Had a Median Driving Range about 60% That of Gasoline Powered Vehicles. 17 January 2022.

[25] United States Advanced Battery Consortium. Goals for Advanced High-Performance Batteries for Electric Vehicle (EV) Applications. 2023.

[26] S. O'Dea. Size of the global battery market from 2018 to 2021, with a forecast through 2030, by technology. *Statista*, 15 January 2023.

[27] Arran Froos. Riddle of 'Baghdad's batteries'. *BBC News*, 20 March 2012.

[28] Wilhelm König. Ein Galvanisches Element aus der Partherzeit? *Forschungen und Fortschritte*, (14):8–9, 1938.

[29] The batteries of Babylon: evidence for ancient eletricity? *Bad Archeology*, 11 November 2016.

[30] E. T. Whittaker. A History of the Theories of Aether and Electricity. *Nelson, London*, 1951.

[31] Marco Bresadola. Medicine and science in the life of Luigi Galvani. *Brain Research Bulletin*, 46(5):367–380, 15 July 1998.

[32] Matthew Li, Jun Lu, Zhongwei Chen, and Khalil Amine. 30 Years of Lithium-Ion Batteries. *Advanced Materials*, 30(33):1800561, 14 June 2018.

[33] Ian D. Johnson, Brian J. Ingram, and Jordi Cabana. The Quest for Functional Oxide Cathodes for Magnesium Batteries: A Critical Perspective. *ACS Energy Letters*, 6(5):1892–1900, 2021.

[34] J. B. Goodenough and Y. Kim. Challenges for rechargeable li batteries. *Chemistry of Materials*, 22(3):587–603, 2010.

[35] Robert C. Massé, Chaofeng Liu, Yanwei Li, Liqiang Mai, and Guozhong Cao. Energy storage through intercalation reactions: electrodes for rechargeable batteries. *National Science Review*, 4(1):26–53, January 2021.

[36] Trading Economics. https://tradingeconomics.com/commodities Date Accessed: 22 July 2023.

[37] Robert Rapier. The World's Top Lithium Producers. *Forbes*, 13 December 2020.

[38] United States Geological Survey. Non-Fuel Mineral Resource Assessment of Afghanistan. 2007.

[39] Victoria Beaule. Artisanal cobalt mining swallowing city in Democratic Republic of the Congo, satellite imagery shows. *ABC News*, 8 February 2023.

[40] Siddharth Kara. Cobalt Red: How the Blood of the Congo Powers Our Lives. *St. Martin's Publishing Group*, 2023.

[41] E-cig explodes in bus passenger's pocket. https://www.youtube.com/watch?v=gG353udgWXM.

[42] Exploding Hoverboard Nearly Sets Family's House on Fire. https://www.youtube.com/watch?v=T2jNHWatZvs.

[43] An Electric Bus Caught Fire After Battery Explosion in Paris. https://www.youtube.com/watch?v=5r-yN8SugWM.

[44] Prateek Hundekar, Rishabh Jain, Aniruddha S. Lakhnot, and Nikhil Koratkar. Recent advances in the mitigation of dendrites in lithium-metal batteries. *Journal of Applied Physics*, 128(1), 2 July 2020.

[45] Yanliang Liang, Hui Dong, Doron Aurbach, and Yan Yao. Current status and future directions of multivalent metal-ion batteries. *Nature Energy*, 5:646–656, 2020.

[46] Claude Delmas. Sodium and sodium-ion batteries: 50 years of research. *Advanced Energy Materials*, 8(17), 2018.

[47] James C. Pramudita, Divya Sehrawat, Damian Goonetilleke, and Neeraj Sharma. An initial review of the status of electrode materials for potassium-ion batteries. *Advanced Energy Materials*, 7(24), 2017.

[48] Adam Z. Weber, Matthew M. Mench, Jeremy P. Meyers, Philip N. Ross, Jeffrey T. Gostick, and Qinghua Liu. Redox flow batteries: a review. *Journal of Applied Electrochemistry*, 41:1137–1164, 2011.

[49] Md. Arafat Rahman, Xiaojian Wang, and Cuie Wen. High Energy Density Metal-Air Batteries: A Review. *Journal of the Electrochemical Society*, 160(10):A1759, 2013.

[50] US Government Accountability Office. Army's Procurement of Batteries: Magnesium vs. Lithium. 26 September 1985.

[51] E.W. Jolie. A Brief History of US Navy Torpedo Development: Torpedo Mk44. 15 September 1978.

[52] D. Aurbach, Z. Lu, A. Schechter, Y. Gofer, H. Gizbar, R. Turgeman, Y. Cohen, M. Moshkovich, and E. Levi. Prototype systems for rechargeable magnesium batteries. *Nature*, 407:724–727, 2000.

[53] CRC Handbook of Chemistry and Physics 97th Edition. Abundance of elements in the earth's crust and in the sea. pages 14–17, 2016-2017.

[54] Rachel Davidson, Ankit Verma, David Santos, Feng Hao, Coleman Fincher, Sisi Xiang, Jonathan Van Buskirk, Kelvin Xie, Matt Pharr, Partha P. Mukherjee, and Sarbajit Banerjee. Formation of magnesium dendrites during electrodeposition. *ACS Energy Letters*, 4(2):375–376, 2018.

[55] Markus Jäckle and Axel Groß. Microscopic properties of lithium, sodium, and magnesium battery anode materials related to possible dendrite growth. *J. Chem. Phys.*, 141(17), 7 November 2014.

[56] Matthew M. Huie, David C. Bock, Esther S. Takeuchi, Amy C. Marschilok, and Kenneth J. Takeuchi. Cathode materials for magnesium and magnesium-ion based batteries. *Coordination Chemistry Reviews*, 287:15–27, 15 March 2015.

[57] John Muldoon, Claudiu B. Bucur, Allen G. Oliver, Tsuyoshi Sugimoto, Masaki Matsui, Hee Soo Kim, Gary D. Allred, Jaroslav Zajicek, and Yukinari Kotani. Electrolyte roadblocks to a magnesium rechargeable battery. *Energy & Environmental Science*, 5(3):5941–5950, 2012.

[58] Wei-Jun Zhang. Structure and performance of LiFePO4 cathode materials: A review. *Journal of Power Sources*, 196(6):2962–2970, 2011.

[59] Arumugam Manthiram. A reflection on lithium-ion battery cathode chemistry. *Nature Communications*, 11(1550), 2020.

[60] P. Barpanda, D. Dwibedi, and S. Ghosh. Lithium metal borate (LiMBO3) family of insertion materials for Li-ion batteries: a sneak peak. *Ionics*, 21:1801–1812, 2015.

[61] K. Momma and F. Izumi. VESTA3 for three-dimensional visualization of crystal, volumetric and morphology data. *Journal of Applied Crystallography*, 44:1272–1276, 2011.

[62] Hugh Glass. Borate polyanion-based systems as Li- and Mg-ion cathode materials. *Apollo - University of Cambridge Repository*, 2017.

[63] D. Van Der Voort, J. M. E. de Rijk, R. van Doorn, and G. Blasse. Luminescence of Rare Earth Ions in Ca3(BO3)2. *Mater. Chem. Phys.*, 31:333–339, 1992.

[64] H. M. Rietveld. A profile refinement method for nuclear and magnetic structures. *Journal of Applied Crystallography*, 2:65–71, 1969.

[65] David Chilton Phillips. William Lawrence Bragg, 31 March 1890 - 1 July 1971. *The Royal Society Publishing*, 25, 1 November 1979.

[66] A. Hewat, W. I F David, and L. van Eijck. Hugo Rietveld (1932-2016). *J. Appl. Cryst.*, 49:1394–1395, 2016.

[67] L. B. McCusker, R. B. Von Dreele, D. E. Cox, D. LoueÈrd, and P. Scardi. Rietveld refinement guidelines. *J. Appl. Cryst.*, 32:36–50, 1999.

[68] Alan A. Coelho. TOPAS and TOPAS-Academic: an optimization program integrating computer algebra and crystallographic objects written in C++. *Journal of Applied Crystallography*, 51:210–218, 2018.

[69] E.I. Kamitsos, A.P. Patsis, M.A. Karakassides, and G.D. Chryssikos. Infrared reflectance spectra of lithium borate glasses. *Journal of Non-Crystalline Solids*, 126:52–67, 1990.

[70] Gerhard Barkleit. Manfred von Ardenne: Self-realization in the century of dictatorships. *Duncker & Humblot*, 2006.

[71] C.W. Oatley. The early history of the scanning electron microscope. *J. Appl. Phys.*, 53:R1–R13, 1982.

[72] S. Mugiraneza and A.M. Hallas. Tutorial: a beginner's guide to interpreting magnetic susceptibility data with the Curie-Weiss law. *Commun Phys*, 5(95), 19 April 2022.

[73] Toyoki Okumura, Yoichi Yamaguchi, Masahiro Shikano, and Hironori Kobayashi. Correlation of lithium ion distribution and x-ray absorption near-edge structure in o3- and o2-lithium cobalt oxides from first-principle calculation. *J. Mater. Chem*, 22:17340–17348, 2012.

[74] Davor Balzar, Nathalie Audebrand, MR Daymond, A Fitch, A Hewat, JI Langford, A Le Bail, D Louër, O Masson, Christopher N McCowan, et al. Size-strain line-broadening analysis of the ceria round-robin sample. *Journal of Applied Crystallography*, 37(6):911–924, 2004.

[75] Ri-Zhu Yin, Yang-Soo Kim, Se-Jong Shin, Inho Jung, Jeom-Soo Kim, and Soon-Ki Jeong. In situ xrd investigation and thermal properties of mg doped licoo2 for lithium ion batteries. *Journal of The Electrochemical Society*, 159(3):A253, 2012.

[76] Qi Liu, Hao He, Zhe-Fei Li, Yadong Liu, Yang Ren, Wenquan Lu, Jun Lu, Eric A. Stach, and Jian Xie. Rate-dependent, li-ion insertion/deinsertion behavior of lifepo4 cathodes in commercial 18650 lifepo4 cells. *ACS Applied Materials & Interfaces*, 6(5):3282–3289, 2014.

[77] V. Aravindan and M Umadevi. Synthesis and characterization of novel LiFeBO3/C cathodes for lithium batteries. *Ionics*, 18:27–30, 2012.

[78] L. Tao, G. Rousse, J. N. Chotard, L. Dupont, S. Bruyère, D. Hanžel, G. Mali, R. Dominko, S. Levasseur f, and C. Masquelier. Preparation, structure and electrochemistry of LiFeBO3: a cathode material for li-ion batteries. *J. Mater. Chem. A*, 2:2060–2070, 2014.

[79] Bao Zhang, Lei Ming, Jun chao Zheng, Jia feng Zhang, Chao Shen, Ya dong Han, Jian long Wang, and Shan e Qin. Synthesis and characterization of multi-layer core–shell structural LiFeBO3/C as a novel Li-battery cathode material. *Journal of Power Sources*, 261:249–254, 2014.

[80] Y.Z. Dong, Y.M. Zhao, Z.D. Shi, X.N. An, P. Fu, and L. Chen. The structure and electrochemical performance of LiFeBO3 as a novel li-battery cathode material. *Electrochimica Acta*, 53(5):2339–2345, 2008.

[81] Prabeer Barpanda, Yasunobu Yamashita1, Yuki Yamada1, , and Atsuo Yamada. High-Throughput Solution Combustion Synthesis of High-Capacity LiFeBO3 Cathode. *Journal of The Electrochemical Society*, 160:A3095, 2013.

[82] Nupur Nikkan Sinha, J.C. Burns, R.J. Sanderson, and Jeff Dahn. Comparative studies of hardware corrosion at high potentials in coin-type cells with non aqueous electrolytes. *Journal of the Electrochemical Society*, 158(12), 2011.

[83] Jianan Xu, Lori Kaufman, Francisco C. Robles Hernández, Atin Pramanik, Ganguli Babu, Jagjit Nanda, Bryan D. McCloskey, and Pulickel M. Ajayan. Effects of ball milling on the electrochemical capacity and interfacial stability of Li2MnO3 cathode materials. *ACS Applied Energy Materials*, 6:5026–5036, 2023.

[84] Semih Afyon, Frank Krumeich, Christian Mensing, Andreas Borgschulte, and Reinhard Nesper. New high capacity cathode materials for rechargeable li-ion batteries: Vanadate-borate glasses. *Scientific Reports*, 4(7113), 2014.

[85] Amorntep Montreeuppathum, Pinit Kidkhunthod, Saroj Rujirawat, Rattikorn Yimnirun, Supree Pinitsoontorn, and Santi Maensiri. Effect of borate glass network to electrochemical properties: Manganese-doped lithium borate glasses. *Radiation Physics and Chemistry*, 170:108677, 2020.

[86] Jidapa lomon, Jintara Padchasri, Amorntep Montreeuppathum, Sumet Siriroj, Yingyot Poo-arporn, Supree Pinitsoontorn, Prayoon Songsiriritthigul, Saroj Rujirawat, Pinit Kidkhunthod, and Narong Chanlek. Effect of ni content in lithium nickel borate glasses: Structure and electrochemical studies. *Journal of Alloys and Compounds*, 911:164994, 2022.

Appendix A

Solid-State Synthesis Reactants

Formula	Chemical	Manufacturer	Purity
MgO	magnesium oxide	Alfa Aesar Puratronic	99.995 (metals basis)
$LiOH{\cdot}H_2O$	lithium hydroxide monohydrate	Alfa Aesar	99.995 (metals basis)
$MnC_2O_4{\cdot}H_2O$	manganese oxalate dihydrate	Alfa Aesar	98% (metals basis)
$NiC_2O_4{\cdot}H_2O$	nickel oxalate dihydrate	Alfa Aesar	98% (metals basis)
$FeC_2O_4{\cdot}H_2O$	iron oxalate dihydrate	Alfa Aesar	96% (metals basis)
H_3BO_3	boric acid	Alfa Aesar	99.99% (metals basis)

Table A.1 Reactants and manufacturers used for solid state synthesis

Appendix B

$Mg_2Mn(BO_3)_2$ Particle Size Data

Digital analysis was performed on SEM images of hand-ground and ball-milled $Mg_2Mn(BO_3)_2$ cathode particles using ImageJ. The average particle widths were 17(10) µm to 6(3) µm for the hand-ground and ball-milled data respectively. The distributions of particle widths are displayed in the dot plot in Figure B.1.

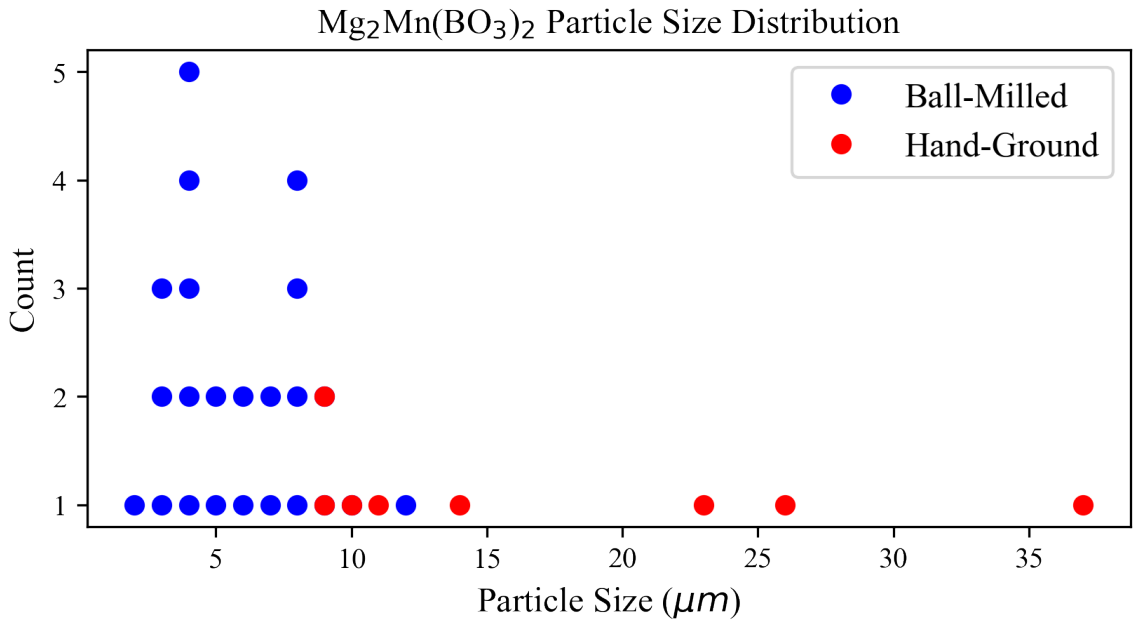

Fig. B.1 $Mg_2Mn(BO_3)_2$ Particle Size Distribution

Appendix C

Synchrotron XRD on Various $Mg_2Mn(BO_3)_2$ States of Charge

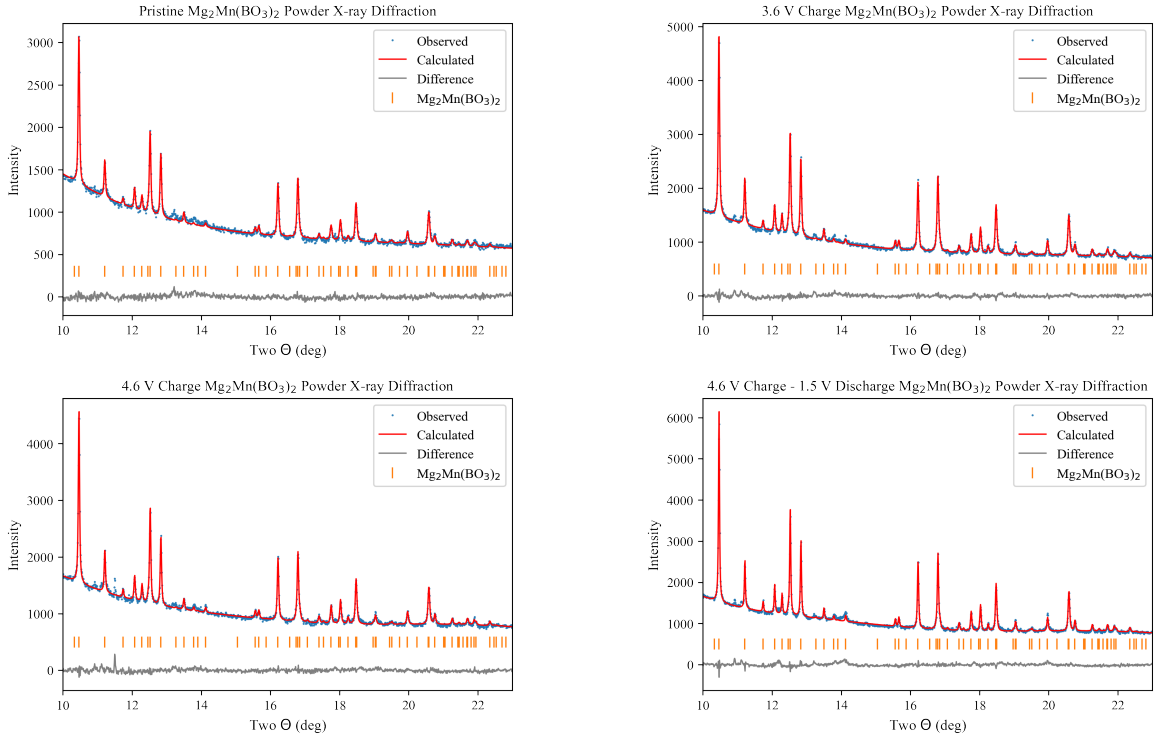

Fig. C.1 $Mg_2Mn(BO_3)_2$ XRD spectra at various states of charge

		Pristine	**3.6 V Charge**	**4.6 V Charge**	**4.6 Charge 1.5 Discharge**
R_{wp}		2.87	2.70	2.60	2.71
a (Å)		5.4836(2)	5.4832(1)	5.4832(1)	5.4831(1)
b (Å)		8.5472(4)	8.5474(2)	8.5470(3)	8.5469(2)
c (Å)		4.5500(2)	4.5499(1)	4.5498(1)	4.5496(1)
Vol ($Å^3$)		213.26(2)	213.24(1)	213.23(1)	213.21(1)
M1 (0, 0, 0)	Occ (Mg/Mn)	0.82/0.18(1)	0.84(1)/0.18	0.83(1)/0.18	0.82(1)/0.18
M2	Occ (Mg/Mn)	0.60/0.40(1)	0.58(1)/0.40	0.59(1)/0.40	0.60(1)/0.40
(0, y, $\frac{1}{2}$)	y	0.3106(4)	0.3111(3)	0.3106(3)	0.3105(2)
B	x	0.255(3)	0.261(2)	0.263(2)	0.259(2)
(x, 0, z)	z	0.541(5)	0.538(3)	0.540(3)	0.542(3)
O1	x	0.311(3)	0.318(1)	0.322(2)	0.322(1)
O2	x	0.203(2)	0.207(1)	0.209(1)	0.2069(8)
(x, y, z)	y	0.1422(9)	0.1373(6)	0.1357(6)	0.1363(5)
	z	0.691(1)	0.6995(9)	0.698(1)	0.6986(8)

Table C.1 $Mg_2Mn(BO_3)_2$ Refined structural parameters for the orthoborates in the *Pnmn* space group. Errors are given in parentheses.

Appendix D

EDX Data on Pristine and Charged $Mg_2Mn(BO_3)_2$ Particles

Particle	Mg Atomic %	Mn Atomic %	x Mg : 1 Mn
Pristine 1	11.5	5.5	2.09
Pristine 2	13.8	6.2	2.23
Pristine 3	8.6	4.6	1.87
Pristine 4	9.7	4.9	1.98
Pristine 5	11.9	5.6	2.13
Pristine 6	8.2	4.1	2.00
Pristine 7	9.1	4.4	2.07
Pristine 8	12.9	5.8	2.22
Pristine 9	13.8	6.7	2.06
Pristine 10	12.6	5.7	2.21
Pristine 11	13.9	6.1	2.28
Pristine 12	9.8	5.3	1.85
Pristine 13	10.9	6.1	1.79
Pristine 14	16.2	7.2	2.25
Charged 1	18.6	7.9	2.35
Charged 2	19.2	8.3	2.31
Charged 3	18.5	8.4	2.20
Charged 4	4.9	2.4	2.04

Table D.1 Atomic percentages and atomic ratios of Mg and Mn in pristine and 4.6 V charged $Mg_2Mn(BO_3)_2$ particles measured using SEM-EDX

Appendix E

$LiFeBO_3$ Synthesis Procedures

Procedure 1: [77]

1. Ball mill stoichiometric amounts of the reactants in acetone for one hour.
    - $LiOH{\cdot}H_2O$, $FeC_2O_4{\cdot}H_2O$, H_3BO_3
    - Zirconia balls in a 10:1 mass ratio with the powder. Acetone fills the vessel to two-thirds volume. Spin at 550 rpm, 7 minutes on, 3 minutes off, repeat 5 times.
2. Let dry in a 29°C oven for 2 hours.
3. Heat the powder to 300°C for 4 hours using a 3°C/min heating rate under the flow of Ar.
4. The resulting amorphous black powder is subsequently pressed into a 13 mm pellet.
5. Heat the pellet to 600°C for 10 hours using a 3°C/min heating rate under the flow of Ar.
6. The pellet is immediately placed in an Ar-filled glove box and hand-ground for further characterization.

Four synthesis attempts. No better than 95% purity was achieved.

Procedure 2: [78]

1. Grind stoichiometric amounts of the reactants with a mortar and pestle.
    - $LiOH{\cdot}H_2O$, $FeC_2O_4{\cdot}H_2O$, H_3BO_3
2. Heat the powder to 250°C for 3 hours using a 3°C/min heating rate.
3. Grind the powder with a mortar and pestle. Press the powder into a 13 mm pellet.
4. Heat the pellet to 750°C for 15 hours using a 3°C/min heating rate under the flow of Ar.

5. The pellet is immediately placed in an Ar-filled glove box and hand-ground for further characterization.

Two synthesis attempts. The intended phase was never produced.

Procedure 3:

1. Grind stoichiometric amounts of the reactants with a mortar and pestle.
    - $LiOH{\cdot}H_2O$, $FeC_2O_4{\cdot}H_2O$, H_3BO_3
2. Heat the powder to 350°C for 10 hours using a 3°C/min heating rate under the flow of Ar.
3. Grind the powder with a mortar and pestle. Press the powder into a 13 mm pellet.
4. Heat the pellet to 650°C for 10 hours using a 3°C/min heating rate under the flow of Ar.
5. The pellet is immediately placed in an Ar-filled glove box and hand-ground for further characterization.

Three synthesis attempts. Greater than 99% purity was achieved.